Monitoring the regional impact of forest loss and gain on carbon uptake with solar-induced fluorescence measurements from the GOME-2A and TROPOMI sensors

Juliëtte C.S. Anema [1,2], Klaas Folkert Boersma [1,2], Piet Stammes [1], Gerbrand Koren [3], William Woodgate [4], Philipp Köhler [5], Christian Frankenberg [6], and Jacqui Stol [7]

[1]Satellite Observations Department, Royal Netherlands Meteorological Institute, De Bilt, 3730 AE, the Netherlands
[2]Meteorology and Air Quality group, Wageningen University, Wageningen, 6700 AA, the Netherlands
[3]Copernicus Institute of Sustainable Development, Utrecht University, Utrecht, 3584 CB, the Netherlands
[4]School of Earth and Environmental Sciences, The University of Queensland, Brisbane, QLD, Australia
[5]EUMETSAT, 64295 Darmstadt, Germany
[6]Jet Propulsion Laboratory, California Institute of Technology, Pasadena, CA 91109, USA
[7]CSIRO Land and Water, Floreat 6913, Western Australia, Australia

Correspondence: Juliëtte Anema (juliette.anema@knmi.nl)

Abstract. Reliable and robust monitoring tools are crucial to assess the effectiveness of land mitigation techniques (LMTs) in enhancing carbon uptake, enabling informed decision-making by policymakers. This study, addressing one of the scientific goals of the EU H2020 LANDMARC project, examines the feasibility of using satellite solar-induced fluorescence (SIF), in combination with other satellite data, as a monitoring proxy to evaluate the effects of LMTs on carbon uptake. Two distinct

5 cases are explored: (1) instantaneous vegetation destruction caused by a 2019 Eucalyptus wildfire in south-east Australia, and, (2) gradual forest gain resulting from reforestation efforts in northern China over 2007–2012. The cases are monitored using TROPOMI and GOME-2A SIF, respectively. Comparing the temporal variability in SIF across the affected and nearby reference areas reveals that vegetation dynamics changed as a consequence of the land use changes in both cases. Specifically, in the Australia case, TROPOMI demonstrated an immediate reduction in SIF signal of 0.6 mW m^{-2} sr^{-1} nm^{-1} (-72 %)

10 over the Eucalypt Forest right after the fire. Exploiting the strong correspondence between TROPOMI SIF and gross primary productivity (GPP) at the nearby eddy-covariance Tumbarumba site and through the FluxSat product, we estimate that the fire led to a loss in GPP of 130-200 GgC in the first eight months after the fire. Over the northern Chinese provinces of Gansu, Shaanxi, Sichuan, Chongqing and Shanxi, we report an increase in GOME-2A summertime SIF of 0.1-0.2 mW m^{-2} sr^{-1} nm^{-1} coinciding with reforestation efforts between 2007 and 2012. This increase in SIF signal is likely driven by a

15 combination of increasingly favourable natural conditions and the reforestation effort itself. A multivariate model that takes into account growth factors such as water availability and maximum temperature as well as satellite-derived forest cover data explains the observed variability in GOME-2A SIF in the Chinese case reasonably well (R^2=0.72). The model suggests that both increases in forest cover as well as in soil moisture have led, in step, to the observed increase in vegetation activity over northern China. In that region, for every 100 km^2 of additional forest cover, SIF increases by 0.1 mW m^{-2} sr^{-1} nm^{-1} between

20 2007 and 2012. Our study highlights that the combined use of satellite-based SIF, together with supporting in situ, modelled

and satellite-data, allows to monitor the impact of LMT implementation on regional carbon uptake as long as the scale of the LMT is of sufficient spatial extent.

1 Introduction

Photosynthetic carbon uptake by the terrestrial biosphere plays a crucial part in the carbon cycle and is the largest flux that
25 contributes to the carbon sink. Over the last 60 years, the terrestrial biosphere captured an amount of carbon equivalent to approximately 32 % of the total anthropogenic emissions in that period (Friedlingstein et al., 2020). However, the ongoing efficacy of this photosynthetic carbon flux, or gross primary productivity (GPP), is not assured due to feedback mechanisms driven by climate change and human activity (e.g. Brook et al., 2013; Huntzinger et al., 2017). Preserving the terrestrial biosphere's pivotal role in dampening the rise of atmospheric CO_2 concentrations is crucial in addressing the current climate
30 crisis. In response to this urgency, land mitigation techniques (LMTs) play a key role as negative carbon technology in national climate strategies (United Nations, 2016) and the climate pathways of the Intergovernmental Panel on Climate Change (Rogelj et al., 2018). These techniques include a variety of practices, such as reforestation and fire management, aimed at enhancing the land's carbon assimilation and preventing carbon stock loss.

The potential of large-scale LMT implementation is exemplified by observed greening trends over actively reforested areas
35 across central to northern China (Chu et al., 2019; Gerlein-Safdi et al., 2020). However, the persisting uncertainty regarding the LMTs' effectiveness in enhancing GPP and carbon sequestration on the long term, limits their widespread implementation (e.g. Harper et al., 2018). The need for robust quantification of changing GPP following land cover change is further emphasized by the uncertain impacts of rising atmospheric CO_2 concentrations and climate change itself on the terrestrial biosphere (Schimel et al., 2015; Smith et al., 2020; Duffy et al., 2021; Schurgers et al., 2018). Understanding the efficiency and applicability
40 of LMTs is essential for effective climate action. Therefore, the Horizon 2020 LANDMARC (Land Use Based Mitigation for Resilient Climate Pathways) project (https://www.landmarc2020.eu/) develops monitoring tools, including satellite-based remote sensing, to study the feasibility of negative emission monitoring and using multiple LMT cases worldwide as test cases.

The recent development of satellite-based measurements of solar-induced chlorophyll fluorescence (SIF) from atmospheric sensors initiated promising opportunities to monitor the GPP dynamics (Frankenberg et al., 2011; Joiner et al., 2011). Chloro-
45 phyll fluorescence (660–850 nm) is the re-emission of the absorbed photosynthetically active radiation (APAR) by the leaf chlorophyll during photosynthesis (Frankenberg and Berry, 2017). The emission of fluorescence dissipates part of the excitation energy from APAR that is not transported to and used by the photochemical reactions in the plant – making both fluorescence and GPP dependent on APAR (Porcar-Castell et al., 2014). SIF measurements depict the captured chlorophyll photons integrated over the canopy within the field of view and thus directly follow the dynamics of photosynthetic activity.
50 Therefore, SIF follows GPP more consistently than traditional greenness parameter observations such as NDVI (e.g. Magney et al., 2019; Gerlein-Safdi et al., 2020).

As part of one of the research objectives of the LANDMARC project, the main goal of this study is to assess the feasibility of satellite-based SIF in combination with other satellite data to monitor the effect of land mitigation techniques (LMTs) on carbon

uptake. Monitoring tools could potentially benefit from the abilities of SIF to track GPP dynamics consistently across various
55 biomes and scales (Zhang and Schwärzel, 2017; Verma et al., 2017; Dechant et al., 2020) and its demonstrated sensitivity to
climate stress (Song et al., 2018; Ač et al., 2015). Previous studies indicated the ability of SIF to evaluate changes in land cover
(Gerlein-Safdi et al., 2020; Guo et al., 2021). However, the use of SIF, aligned with supporting satellite data, to quantify the
isolated effect of land use change on GPP has not been assessed to our knowledge.

Here, we use TROPOMI and GOME-2A SIF to monitor two cases of forest cover change. First, we use monthly TROPOMI
60 SIF to track the aftermath of a 2019 wildfire in south-east Australia, impacting around 210 km^2 of Eucalypt forest. Next, we use
summertime GOME-2A SIF to monitor multi-year reforestation efforts in northern China from 2007 to 2012. The Australian
case acts as a proof-of-concept due to its immediate and distinct, single-cause land cover change, while the Chinese case tests
how SIF can be used to monitor the combined effect of gradual forest cover change and variability in growth conditions (water
and radiation availability) (Gao et al., 2019; Lin et al., 2020; Wang et al., 2022). Satellite-based data, including MODIS burned
65 area and landsat-derived annual land cover data, are used to evaluate the spatial and temporal extent of the changed forest cover
in both cases. Subsequently, a comparative analysis between the impacted and reference area was conducted.

Our study addresses the following research questions: (1) Is it possible to monitor changes in vegetation dynamics that
are linked to instantaneous or gradual land cover changes over scales that can be resolved by the TROPOMI and GOME-2A
sensors?, (2) how can we quantify the impact of instantaneous land use change on carbon uptake?, and (3) how can we use
70 remotely sensed metrics to improve our understanding of climate variability and forest cover change on interannual SIF?

2 Data

2.1 Space-based SIF observations

Satellite measurements of SIF are powerful, near-daily proxies of vegetation growth, and they have been used in many studies
to monitor the changes in GPP. Retrieval of SIF from satellite measurements, from e.g. GOME-2A and TROPOMI, rely on
75 the relative in-filling of solar Fraunhofer lines in the Earth's radiance spectra. The apparent depth of the Fraunhofer lines is
not affected by scattering or reflection from clouds or the Earth's surface. However, if vegetation is present at the surface,
the addition of solar-induced fluorescence (SIF) as a spectrally continuous surface light source, dampens the relative depth
of the lines, and this (relative) in-filling of the Fraunhofer lines is a measure for the strength of fluorescence (Joiner et al.,
2011; Frankenberg et al., 2011). The spectral fitting window is selected wide enough to cover multiple strong Fraunhofer
80 lines and sufficiently narrow as to limit the presence of atmospheric absorption features. Spectral basis functions derived
from observations over vegetation-free, non-fluorescent areas are used to describe the impact of atmospheric interaction and
possible instrumental artifacts – the reference set. Accordingly, the SIF signal is computed through the fitting of the satellite-
observed spectrum with a modeled reflectance spectrum, assembled from the spectral basis functions. Uncertainty in the SIF
data emerges from measurement noise, the presence of optically thick clouds in the satellite field-of-view and the fitting
85 procedure, the latter depending on the quality and representativeness of the spectral basis functions.

2.1.1 SIF retrieved from TROPOMI

In this study, we use level-2 SIF (at 740 nm) data retrieved from the TROPOspheric Monitoring Instrument (TROPOMI) by Caltech (Köhler et al., 2018). TROPOMI is an atmospheric spectrometer onboard the Sentinel-5 Precursor that performs in a wide spectral range from the ultraviolet to the shortwave-infrared. The instrument was launched on the 13th of October 2017 and flies in a low earth, polar, sun-synchronous orbit with equatorial crossing at 13:30 local solar time (LST) and with a repeat cycle of 17 days (Veefkind et al., 2012). The 2600 km wide swath enables almost daily global coverage. TROPOMI SIF, with a spatial resolution of 7×3.5 km^2 at nadir, is retrieved from a subset of the NIR band with a selected window ranging from 743 to 758 nm. TROPOMI SIF has a single-pixel 1-σ uncertainty in the range of 0.3–0.5 mW m^{-2} sr^{-1} nm^{-1} (Köhler et al., 2018).

TROPOMI SIF has been previously used to track photosynthetic activity following extreme precipitation events in the US (Turner et al., 2021), dry-season in the Amazon forest (Doughty et al., 2019), and over evergreen forests (Magney et al., 2019). Furthermore, it is extensively validated with GPP from multiple eddy-covariance towers and OCO-2 SIF (Li and Xiao, 2022; Köhler et al., 2018). Until ESA's FLEX mission will be launched (in 2025), with a spatial resolution of 300 m (Drusch et al., 2016), TROPOMI SIF is arguably the most appropriate data product to track photosynthetic activity from vegetation on a global scale from space. The main limiters for detecting the impact of LMTs on vegetation activity are the spatial scale of a TROPOMI pixel (±20 km^2) and the data not being available before April 2018.

2.1.2 SIF retrieved from GOME-2A

We also use clear-sky gridded (level-3) SIF data from KNMI's SIFTER v2 product (Kooreman et al., 2020; Van Schaik et al., 2020) retrieved from the Global Ozone Monitoring Experiment-2A (GOME-2A) sensor. The data has a spatial resolution of $0.5° \times 0.5°$. GOME-2A was launched on 6 November 2006 onboard Metop-A and flies in a sun-synchronous orbit with equatorial crossing at 09:30 LST. The GOME-2A swath covers 1920 km, resulting in the spatial resolution of 80×40 km^2 in nadir. Due to a swath reduction on 15 July 2013, the spectral resolution thereafter was 40×40 km^2. Despite the 160 times coarser resolution of GOME-2A in comparison to TROPOMI, the GOME-2A SIF data is of relevance due to the long temporal record, starting from 2007. The GOME-2A SIF product is retrieved from a subset of band 4 with a selected window ranging from 734 to 758 nm and the SIFTER retrieval principle is similar to that of TROPOMI SIF. GOME-2A SIF has a single-pixel uncertainty on the order of 0.6 mW m^{-2} sr^{-1} nm^{-1} (Van Schaik et al., 2020). The retrieval is considered most reliable in the period before the sensor switch in July 2013 (Van Schaik et al., 2020). After the July 2013 switch, degradation of the GOME-2A sensor and subsequent calibration updates in different level-1 data versions have posed difficulties in deriving a consistent, bias-free data record. Post-hoc degradation corrections, introduced in Van Schaik et al. (2020), have (at least partly) improved the consistency of the GOME-2A SIF data record in the post-2013 years.

We exclusively use the GOME-2A data from the years 2007–2012 for two main reasons. Firstly, this enables a constant satellite viewing geometry throughout the analyzed time series. Secondly, we hereby limit level-1 calibration issues associated with strong instrument degradation and unresolved differences in level-1 calibration post-processing within the data set (Van

Schaik et al., 2020; Gerlein-Safdi et al., 2020). Additionally, we applied a year-specific multiplicative correction to the SIF-
120 data, addressing the effect of instrument degradation on SIF. The corrections are determined over China's Gobi Desert, where
vegetation is mostly absent, and a constant near-zero SIF signal is expected. Appendix B describes the correction procedure in
detail, and we note here that the (multiplicative) correction factors have values between 0.85 and 1.12, and that their application
improves the correspondence between GOME-2A SIF and FluxSat GPP over northern China (Fig. B3).

Various applications have shown data to be of good use for detecting the effects of heatwaves on GPP in Europe (Wang et al.,
125 2020), quantifying GPP over Africa (Getachew Mengistu et al., 2021), and to map the impact of El Nino on forest productivity
in the Amazon (Fancourt et al., 2022). GOME-2A SIF has been validated with GPP from various eddy-covariance flux towers
in Africa (Getachew Mengistu et al., 2021).

2.2 Gross primary productivity (GPP) data

2.2.1 GPP from Tumbarumba flux tower

130 This study uses estimated GPP data from the Tumbarumba OzFlux eddy covariance flux tower site as ground-reference to the
TROPOMI SIF observations (AU-TUM: 35.66° N, 148.15° E) (Stol and Kitchen, 2022). The Tumbarumba site is located in
the Bago State forest and is predominated covered by Eucalyptus forest. GPP is not directly measured, but calculated using
partitioning methods by the extraction of modelled respiration from the measured net ecosystem exchange (NEE) of CO_2. NEE
at the site is quantified using the eddy covariance method, which involves simulteously measuring vertical wind speed and
135 CO_2 concentration (Moene and Van Dam, 2014).

For our analysis, we use the quality-checked and gap-filled daily GPP (in gC m^2 day^{-1}) from the L6 data. The Tumbarumba
data is processed following the standard tool developed by OzFlux, which is described in more detail in Isaac et al. (2017). To
match the recording time of TROPOMI SIF and account for the impact of the Dunn-road fire that affected the OzFlux site in
December 2020, GPP data between February 2018 and November 2020 are used.

140 ### 2.2.2 FluxSat GPP product

The modelled global FluxSat GPP product is used as independent GPP data to compare against SIF and the OzFlux GPP data
for the Australia case study. The data set contains daily averaged GPP estimates (gC m^{-2} day^{-1}) at a spatial resolution of 0.05°
× 0.05° over the period March 2000 to August 2020. The FluxSat GPP product is found to agree well with GPP from flux
towers (Joiner et al., 2018), TROPOMI-inferred GPP (Turner et al., 2021), and has previously been used to quantify changes
145 in carbon uptake (e.g. Byrne et al., 2021; Bacour et al., 2019).

The global FluxSat GPP (Joiner et al., 2018) product is derived from the evaluation and training of satellite data-driven mod-
els that are based on the light use efficiency concept (Monteith, 1972), which states linearity between GPP and the absorbed
photosynthetically active radiation. MODIS reflectance (MCD43) data serve as vegetation indices input for the model. Fur-
thermore, the models are trained and calibrated using a subset of eddy-covariance flux data obtained that contained data across
150 various plant types. In addition, GOME-2A SIF (v27) (Joiner et al., 2013, 2016), a different SIF-product from NASA, is used

in the FluxSat calibration procedure to delineate highly productive regions that are not well fitted and underestimated using the global regression model. Guanter et al. (2014) found high GPP values from cropland to deviate from the linear relation. Therefore, high productive regions were trained and calibrated separately using a eddy-covariance GPP subset that met the high SIF and GPP criteria (Joiner et al., 2018). As GOME-2A SIF is merely used to identify productive areas, FluxSat GPP
155   estimates remain largely independent from SIF.

3   Forest loss following Eucalyptus fire in South-East Australia

We first investigate the case of a 2019 Eucalyptus wildfire in southeastern Australia to evaluate the ability of SIF to capture the fire-induced change in vegetation dynamics. Lightning strikes on 16 January 2019 ignited multiple fires across remote, forested areas in Victoria, South-East Australia. Strong northwesterly winds propagated and coalesced several individual fires
160   into a clustered Eucalyptus fire, which is locally known as the Nunnett-Timbarra River Fire following its extent between the Nunnett State Forest and the Timbarra river. Burning for nearly 4 weeks, the wildfire impacted around 210 km^2 of Eucalyptus forest spanning from 148.0–148.2° E and 37.35–37.2° S. The impacted area was not previously affected by wildfires within the 25 years prior to the event (Lindenmayer and Taylor, 2020). The fire has been documented to have caused a sharp reduction of leaf biomass in January 2019, but left Eucalypt tree stems and branches mostly intact, according to witness reports by the
165   Australian Forestry Service.

Figure 1 shows the location of the area impacted by the Nunnett-Timbarra River Fire in the context of the wider biogeography of South-East Australia. Figures 1c and d show that prior to the fire (April 2018), the area enclosed by the solid line – that would burn down in early 2019 – as well as the surrounding area bound by the dashed line – that was spared from the fire – had high levels of SIF and GPP, indicating vigorous growth conditions in both areas under normal circumstances.
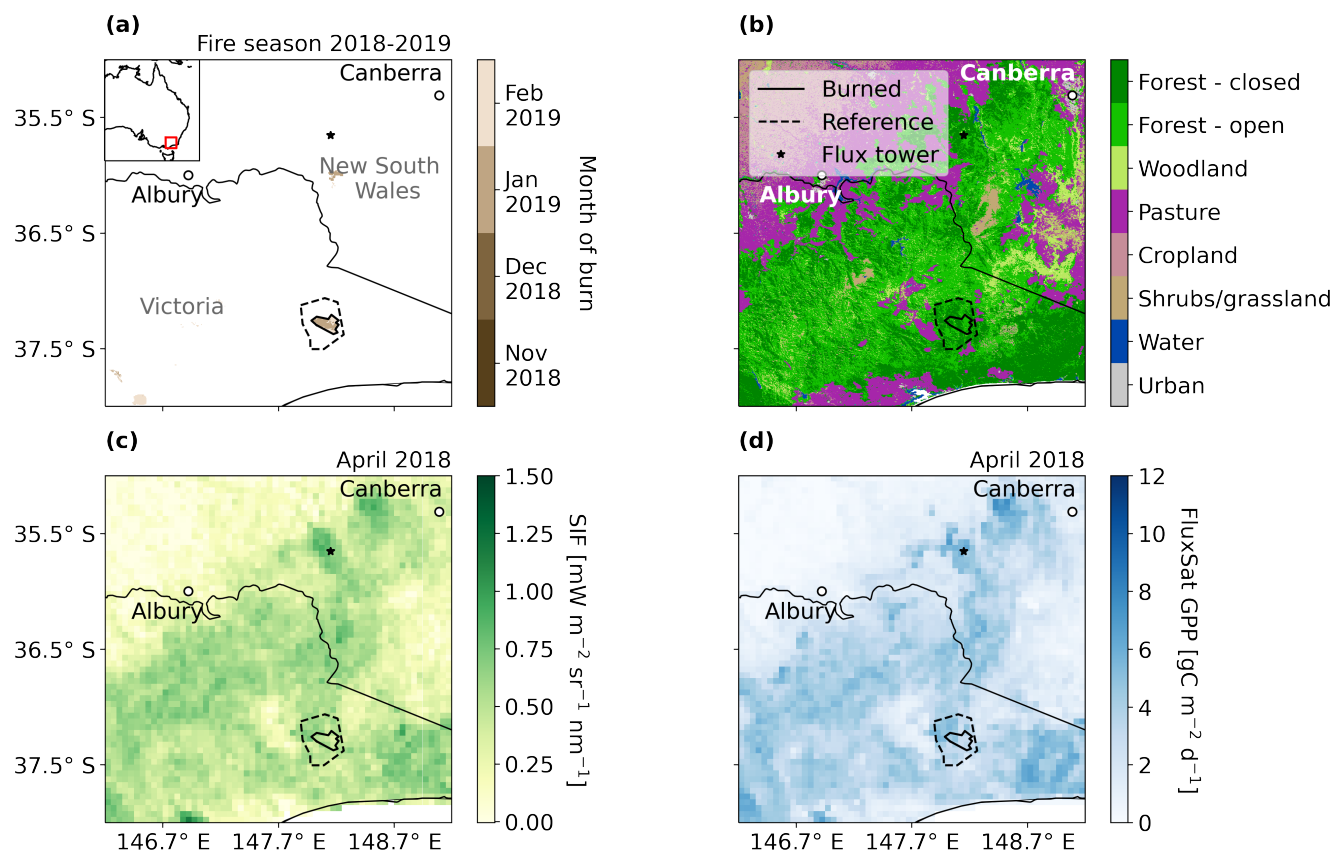
Figure 1. Location and extent of the Nunnett-Timbarra River Fire and selected reference area. Maps of (a) the burned area per month of burn from the MODIS MCD64A1 Burned Area product (Giglio et al., 2015), (b) dominant land cover over the area with classification based on the 2015 Land Cover Dataset (Lymburner et al., 2015), (c) monthly mean TROPOMI SIF ($0.05° \times 0.05°$), and (d) monthly mean of FluxSat GPP ($0.05° \times 0.05°$) over April 2018. The outline of the burned (approximately 210 km^2) and reference area (approximately 975 km^2) are indicated by the solid and dashed line, respectively. Location of the Tumbarumba OzFlux site (AU-TUM) used in this study is shown as a black star.

3.1 Reduction in SIF following the Eucalyptus forest fire

We evaluate the spatial and temporal trends in TROPOMI SIF over the burned area from February 2018 until November 2020. The monitoring period ends in November 2020 to avoid potential interference from subsequent wildfire events that occurred in December 2020 and affected the studied region (Bowman et al., 2021). The extent of the Eucalyptus fire is identified using the MODIS MCD64A1 Burned Area monthly product (Giglio et al., 2015) (Fig. 2a), and the impacted burned area is defined as the region encompassing the MODIS burned pixels, indicated by the solid lines in Fig. 1 and 2a and b. Next, for comparison, we carefully selected a reference area surrounding the burned area that remained unaffected by the fire. This reference area was chosen to closely match the biogeography of the impacted area, consisting of a mixture of open and close Eucalyptus forest

(Fig. 1b). SIF observations over the reference area are assumed to represent the forest dynamics over the burned area as if the fire had not taken place.

180   To evaluate temporal trends in SIF over both areas, we categorized TROPOMI L2 pixels as either 'burned' or 'reference' based on their spatial overlap with each respective area. Criteria were implemented for each group to ensure pixel exclusivity and minimize interference. Pixels are labelled as 'burned', if the burned area fraction exceeded 50 %. Pixels are labelled as 'reference' if they comprised less than 30 % of burned area. Subsequently, within each group, the SIF values were averaged on a monthly basis. Note that throughout the reporting of the results, all uncertainty values are stated in standard error (SE).
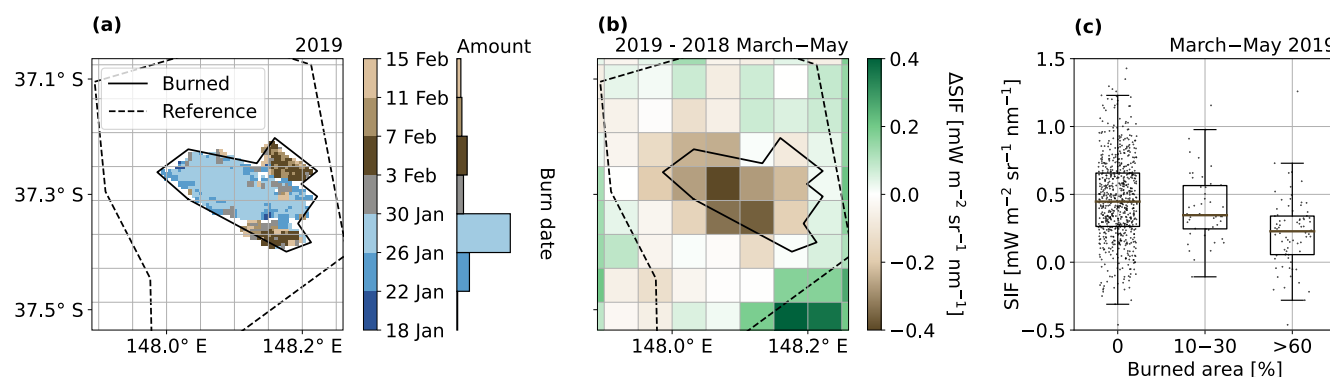
Figure 2. Impact of the 2019 Eucalyptus fire on TROPOMI SIF over time and in comparison to the unburned reference area and pre-fire conditions. Map of (a) the burned areas and their specific burn data at 1 km scale from the MODIS MCD64A1 Burned Area product, and (b) the difference in SIF between post (2019) and pre-fire (2018) conditions over March–May (Autumn). Brown indicates higher SIF in 2018 (pre-fire), green indicates higher SIF in 2019 (post-fire). (c) Correlation between SIF over March–May 2019 (post-fire) and the coverage of the 500-m burned area pixels by the SIF pixels, in percentage.

185   Figure 2b shows the difference in TROPOMI SIF between 2019 (post-fire) and 2018 (pre-fire), specifically over the Autumn months March–May. Over the area that burned down, autumnal SIF values in 2019 decreased significantly compared to 2018. In contrast, SIF at the reference area remained consistent across both years. Furthermore, the lowest SIF values (0.25 mW m^{-2} sr^{-1} nm^{-1}) coincide with pixels with burned area fractions higher than 60 %, whereas SIF is much higher (0.45 mW m^{-2} sr^{-1} nm^{-1}) in pixels that had not burned, as illustrated in Fig. 2c. We conclude that TROPOMI SIF is capable of capturing the

190 strong reduction in vegetation activity over the burned area relative to the unburned reference area, noting that the affected area extends over some 200 km^2, equivalent to 8 individual TROPOMI pixels.
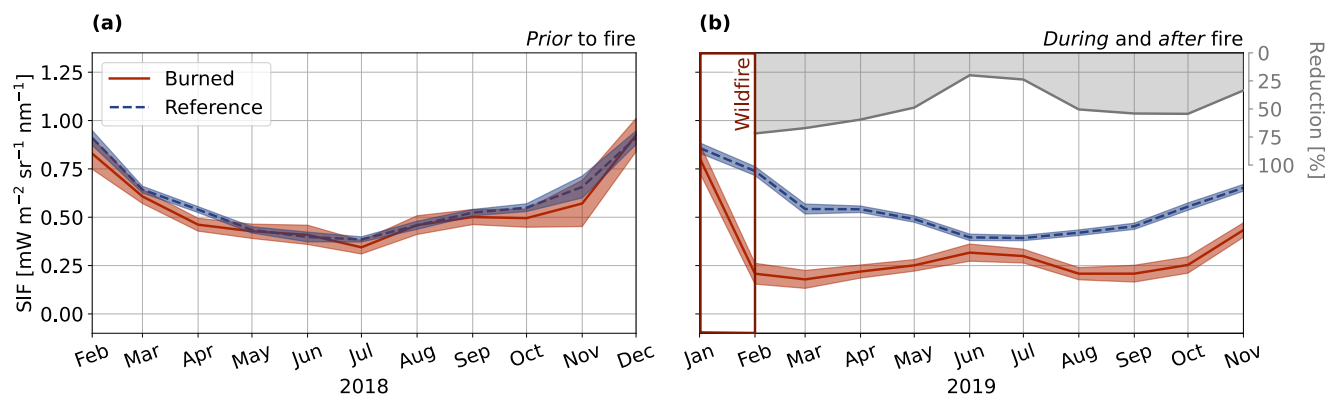
Figure 3. Time series of SIF over the burned and reference area (a) prior to the fire in 2018 and (b) during and after the fire in 2019. The shaded red and blue area represents the standard error (SE) in monthly SIF over the burned and reference area, respectively. The right y-axis of plot (e) shows the reduction in SIF (in %) over the burned area (F_{B}) as compared to SIF over the reference area (F_{R}), which is calculated as $1\text{-}\frac{F_{\mathrm{R}}-F_{\mathrm{B}}}{F_{\mathrm{R}}}$. Prior to monthly averaging, SIF pixels beyond $\pm 2\sigma$ from their respective seasonal group mean were removed.

Figure 3a shows the seasonal cycle in 2018 (pre-fire) inferred from TROPOMI SIF over the to-be burned and reference area. Prior to the fire event, the observed SIF values indicate consistency and a strong agreement between the two areas (r=0.97, Fig. A1a). However, shortly after the fire, a substantial reduction in SIF over the burned area becomes evident (Fig. 3b). This immediate fire-induced impact is highlighted by a striking 72 % decrease in February SIF values compared to the reference area. In the subsequent months, the vegetation activity over the burned area remained low, but non-zero, with averaged SIF of 0.26 ± 0.01 mW m^{-2} sr^{-1} nm^{-1} between February and August 2019. During springtime (September–November), vegetation recovery was noticeable with SIF values reaching 0.43 ± 0.04 mW m^{-2} sr^{-1} nm^{-1} by November. In fact, the SIF grew faster in springtime over the burned area than were over the reference area, with respective increases of 208 % and 144 %, hinting at accelerated regrowth in a moderately burned area that was also reported in Zambia and Alaska (Chungu et al., 2020; Madani et al., 2021).

3.2 Quantifying the fire-induced reduction in GPP

Next, based on the observed reduction in SIF, we quantify the fire-induced reduction in GPP. Previous studies found space-based SIF observations to be proportional to GPP at canopy scale. This proportionality is defined by biome-specific linear relationships that are widely used to scale SIF to GPP (e.g. Turner et al., 2020; Liu et al., 2017; Sun et al., 2018). Building upon this recognized relationship between SIF and GPP, we assume that the relative reduction in SIF (Sect. 3.1) represents the loss in GPP (ΔSIF$\propto\Delta$GPP). Consequently, we express the fire-induced change in GPP over the burned area, $\Delta M_{\mathrm{B}}(t)$ (in gC m^{-2} day^{-1}) over month t as the product of the relative change in SIF ($\Delta F_{\mathrm{B}}(t)$) and 'baseline' GPP ($M_{\mathrm{R}}(t)$) over the reference area (as if no fire had occurred):

$$\Delta M_{\mathrm{B}}(t) = \Delta F_{\mathrm{B}}(t) M_{\mathrm{R}}(t) \tag{1}$$

To compute the SIF-based GPP over the reference area (M_R (t)), we first characterize the SIF–GPP relationship using GPP data from a representative eddy-covariance site (see Appendix A). Specifically, GPP data from the nearby Tumbarumba (AU-TUM) site (Stol and Kitchen, 2022) is used to compare against TROPOMI SIF. We obtain the SIF-based GPP over the reference area as:

$$M_{\mathrm{R}}(t) = F_{\mathrm{R}}(t)\frac{M_{\mathrm{TUM}}}{F_{\mathrm{TUM}}} \tag{2}$$

215

where F_R (t) represents the SIF evolution over the reference area, and $\frac{M_{\mathrm{TUM}}}{F_{\mathrm{TUM}}}$ is the local SIF–GPP relationship over the Tumbarumba flux site. We hold the SIF–GPP relationship over Tumbarumba to be applicable to our study area due to the similar biogeography of lowland Eucalypt forest over both areas (Fig. 1b). This is supported by the strong spatiotemporal correlation between TROPOMI SIF over Tumbarumba and the reference area in the year prior to the fire (r=0.92), and also by the good correlation between FluxSat GPP estimates over Tumbarumba and the reference area in the year prior to the fire (r=0.79) (Fig. A1b and c).

220

As an alternative, we also compute SIF–GPP relationships over Tumbarumba from TROPOMI SIF and modeled FluxSat GPP, because flux towers are known to have a relatively small spatial footprint and capture mostly local rather than regional GPP. The temporal dynamics of TROPOMI SIF exhibit strong consistency with both the GPP estimated from eddy-covariance flux tower data (r=0.91) as well as the modelled (FluxSat) GPP (r=0.94), providing some confidence in both estimates. Yet, the SIF–GPP relationship based on the flux tower GPP measurements is a factor 2 stronger than the relationship based on the FluxSat GPP data (Table A1, Fig. A2a). The factor 2 difference in SIF-GPP relationship arises from different spatial footprints between the FluxSat model (a much more spatially extended GPP estimate) and flux tower GPP, which measures a more local GPP signature, almost a factor 2 higher GPP than FluxSat (Fig. A2b), and inherent uncertainties and biases in the estimates of the FluxSat GPP product.

225

230

Finally, we estimate the reduction in GPP employing SIF–GPP relationships that use (1) OzFlux GPP data and (2) FluxSat GPP data over Tumbarumba. Additionally, we compute the reduction in GPP (3) from the FluxSat GPP data directly over the burned and reference area. Figure A3 in the appendix shows an overview of the three approaches to compute ∆GPP.
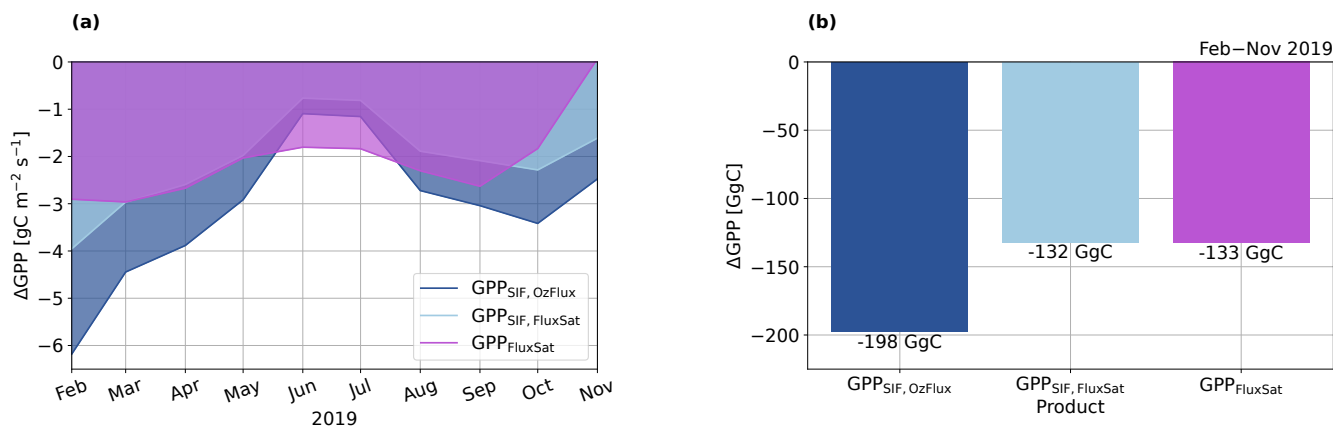
Figure 4. Reduction in GPP following from the Eucalyptus wildfire over the first eight months post-fire (Feb–Nov 2019). (a) Time series of reduced GPP and (b) barplot of total reduction as obtained from SIF-based GPP using OzFlux data from the Tumbarumba site, SIF-based GPP using FluxSat GPP over Tumbarumba, and FluxSat GPP, shown in dark blue, light blue and purple, respectively.

Figure 4a shows the obtained fire-induced reductions in GPP over time. The SIF-based approaches in blue show a sharp
235   reduction in GPP immediately after the fire, followed by smaller GPP deficits in winter, when vegetation activity is low. The FluxSat data also shows a direct local impact of the wildfire on GPP. However, the fire-induced loss is lower and less pronounced than observed through the SIF-based approaches. Moreover, the FluxSat data suggest complete recovery in November in contrast to our SIF-based results. Integrated over February–November 2019 and over the burned area, we find SIF-based GPP losses of 198 GgC and 132 GgC (48 %) using SIF–GPP relationships from the Tumbarumba flux tower and FluxSat
240   product, respectively (Fig. 4b). Thus, we estimate a SIF-based loss in the range of 130–200 GgC over the initial eight months post-fire. For comparison, FluxSat GPP provides a fire-induced loss of 133 GgC over the monitored period, a reduction of 58 % compared to FluxSat GPP in February–November 2018.

One uncertainty in our approach may arise from using SIF–GPP relationships at Tumbarumba, where no fire occurred, to drive our GPP-loss estimate via Eq. (2) over the Nunnett-Timbarra River area that burned down. For comparison, we therefore
245   calculated the SIF–GPP relationships over the Nunnett-Timbarra River area, both prior and posterior to the fire. The (TROPOMI SIF – FluxSat GPP) relationships are within 14 % of those reported over Tumbarumba (Table A1), well within the factor of 2 difference discussed earlier. We conclude that estimating changes in GPP based due to land cover changes is well possible with TROPOMI SIF in combination with empirical SIF–GPP relationships, at least when such land cover changes occur over a spatial scale of a few hundred km^2.

250   ## 4 Reforestation in north-central China

We now turn to examining how GOME-2A can be used to monitor the impact of reforestation on carbon uptake in parts of northern China. Our study area includes the Shaanxi province, southwestern Shanxi, eastern Gansu and part of northern

Sichuan and Chongqing. This region spans approximately 31° to 38° N and 105.0° to 111.5° W (Fig. 5a). Over the past 15 years, the area has undergone various greening campaigns like the Grain for Green, the Natural Forest Conservation Program
255 and the Three-North Shelterbelt Program (Delang and Yuan, 2015; Kong et al., 2021). These efforts have led to observable positive trends in vegetation activity (Gerlein-Safdi et al., 2020; Lin et al., 2020; Li et al., 2015; Sun et al., 2015; Cao et al., 2009).
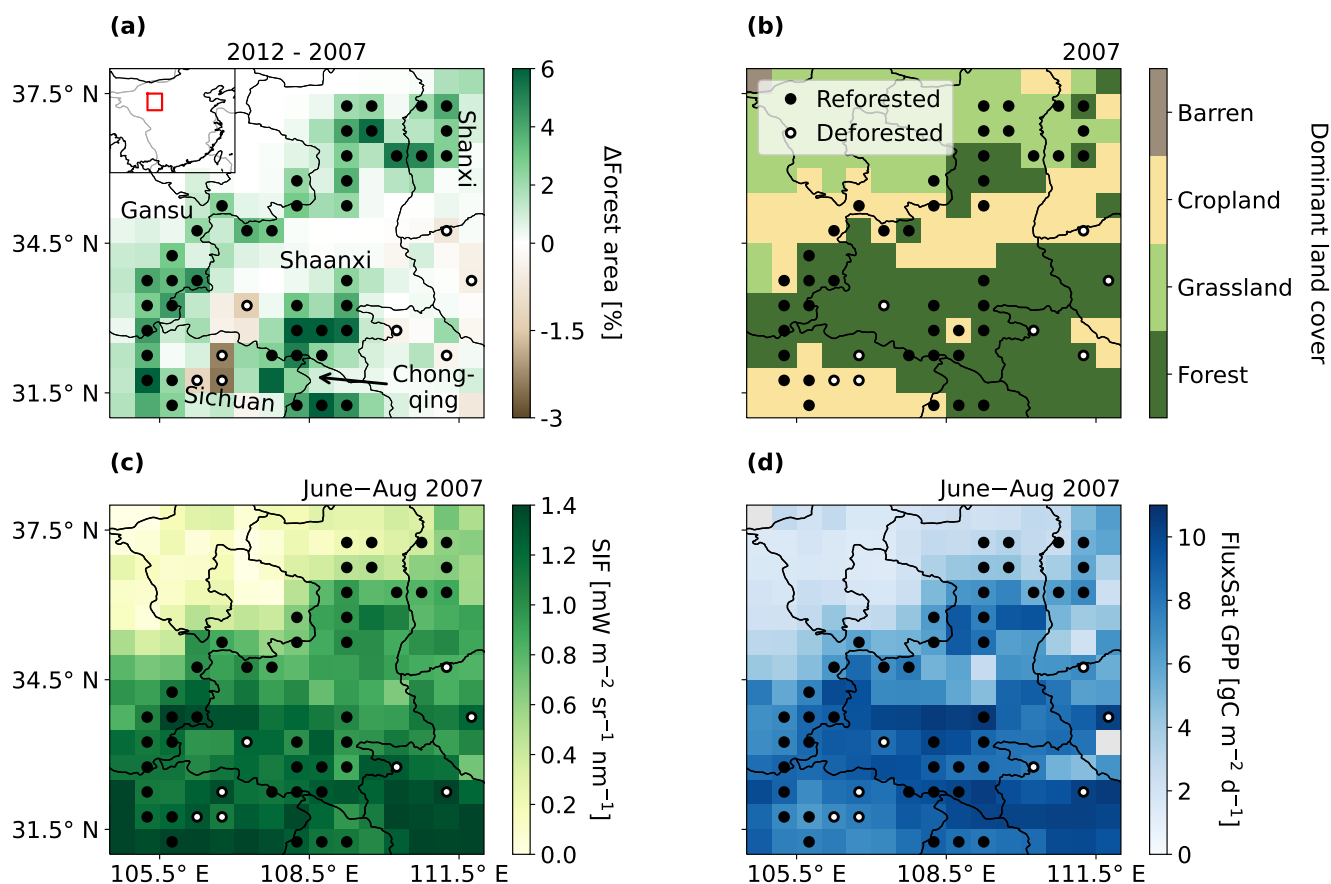
Figure 5. Location and extent of the reforestation efforts between 2007 and 2012 over the study region in northern China. Maps of (a) changed forest cover in 2012 with respect to 2007 (in % of cell area) obtained from the China land cover dataset (CLCD) (Yang and Huang, 2021), with green indicating higher forest coverage in 2012 (reforestation) and brown indicating larger forest coverage in 2007 (deforestation), and (b) dominant land cover in 2007 with classification based on the CLCD, aggregated over the 0.5° × 0.5° GOME-2A SIF grid. Croplands are shown in yellow, grasslands in light green and forests in dark green. Maps of (c) GOME-2A SIF and (b) FluxSat GPP, averaged over summertime (June–Aug) 2007. Selected reforested cells and deforested cells are indicated by black and white-faced bullets, respectively.

Figures 5a and b show that most of the forest gain occurred within and at the borders of the Shaanxi province, and predominantly over area dominated by forest or cropland cover, as diagnosed with the Landsat China land cover dataset (Yang and

260 Huang, 2021). Figures 5c and d show that high summertime average GOME-2A SIF and FluxSat GPP values generally occur in the vegetated southern part of the domain, including the regions where reforestation has taken place, whereas lower average SIF and GPP values are observed in the dryer northern part of the region.

4.1 Coinciding increase in forest cover and SIF

We first examine the 2007–2012 variability in summertime (June–August) GOME-2A SIF, when vegetation productivity is
265 maximum. To evaluate the changes in SIF, we used the first Landsat-derived annual China land cover dataset (CLCD) (Yang and Huang, 2021). This satellite-based data categorizes nine major land types, such as cropland, forest, and grassland, at a spatial resolution of 30 m. Specifically, we extracted forest coverage data for each year between 2007 and 2012, aggregated over the $0.5° \times 0.5°$ GOME-2A SIF grid. The conversion to forest, from any type of land cover, was determined by quantifying the change in forest cover relative to the 2007 baseline. We then compared changes in summertime SIF between 2007 and 2012
270 over two contrasting groups of cells: reforested n=42) and deforested (n=8). We classify cells as 'reforested' if they gained more than 2 % of their area in forest coverage (approximately 50 km^2), and as 'deforested' (n=8) if they lost forest coverage during this period as shown in Fig. 6a. Cells in both groups consistently gained or lost forest coverage annually with every passing year from 2007 to 2012.

The majority of reforested cells show an increase in average summertime SIF, whereas most deforested cells experienced a
275 decrease (Fig. 6b). Figure 6c shows the clear contrast in SIF trends across cells that gained forest compared to those that lost forest coverage. Reforested cells exhibited significant increase in SIF with 0.17 ± 0.03 mW m^{-2} sr^{-1} nm^{-1}, while SIF decreased with 0.09 ± 0.07 mW m^{-2} sr^{-1} nm^{-1} over the deforested cells between 2007 and 2012. The contrasting trend in vegetation activity indicated by GOME-2A SIF over the reforested and deforested cells is confirmed by co-sampled, independent data from NIRv and FluxSat GPP (Fig. 7a and b).
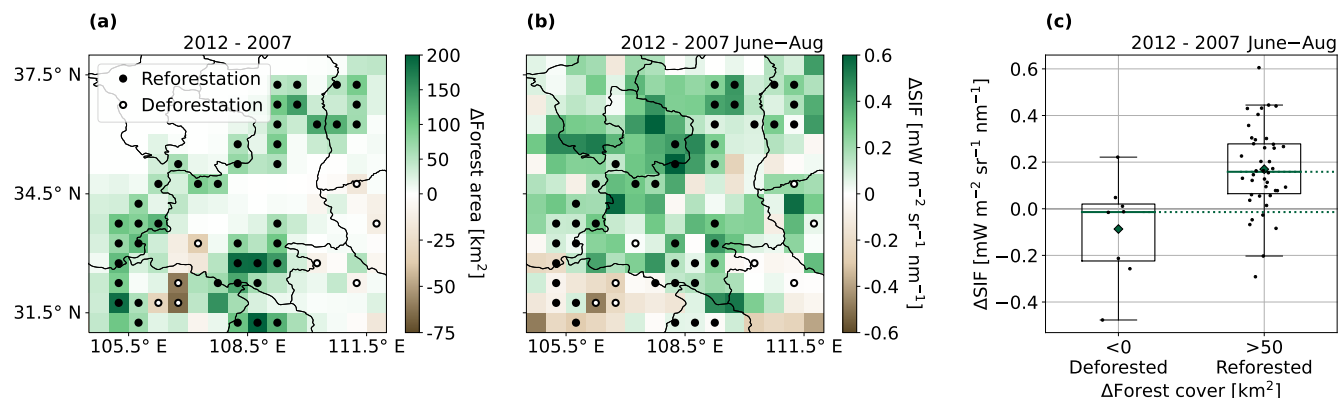
Figure 6. Impact of increased forest coverage in northern China between 2007 and 2012. Maps of changed (a) forest coverage (in km^2) calculated from the China land cover dataset (Yang and Huang, 2021) and (b) summertime GOME-2A SIF over the six years. Green indicates higher forest coverage/SIF in 2012 and brown indicates higher forest coverage/SIF in 2007. (c) Contrast in GOME-2A SIF trend between 2007 and 2012 over the deforested and reforested cells. The reforested and deforested cells are indicated by black and white-faced bullets in (a) and (b).
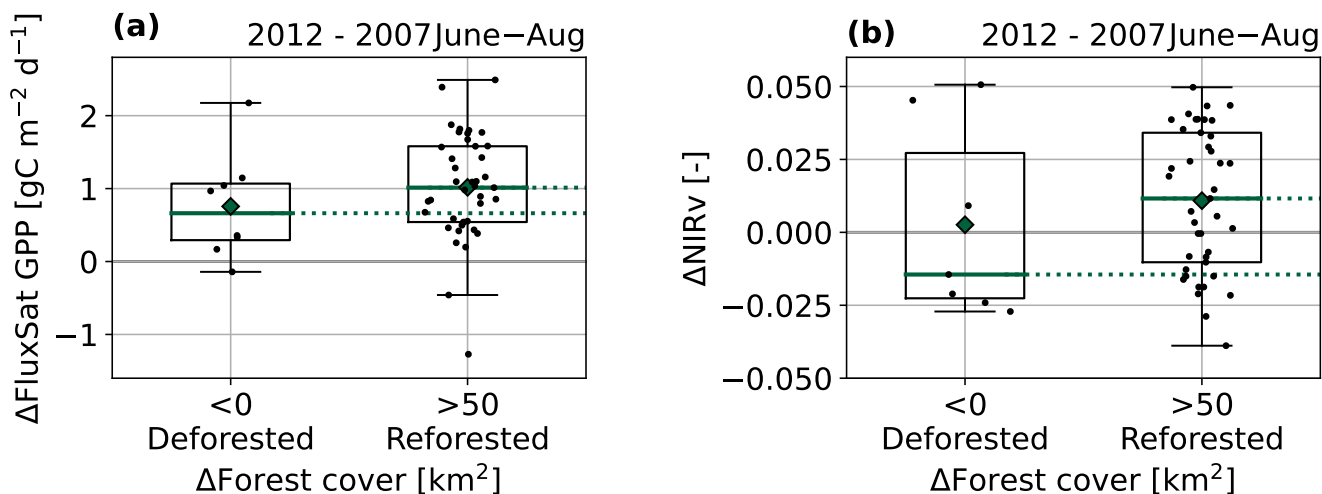
Figure 7. Contrast between deforested and reforested cells in changed vegetation activity between 2012 and 2007, shown using (a) FluxSat GPP, and (b) the near-infrared reflectance of vegetation (NIRv) retrieved from MODIS.

Temporal SIF variability across northern China is not driven by reforestation alone, but also by co-occurring changes in local climate factors that influence plant growth, such as water availability, heat, and the presence of photosynthetically active radiation (Zhang and Ye, 2021; Gao et al., 2019; Lin et al., 2020). To examine the concurring impact of climate variability and changes in forest cover, we use satellite-based soil moisture and maximum temperature. Soil moisture data was obtained from the Surface Soil Moisture (Active) product (Dorigo et al., 2019) and the daily maximum temperature was derived from hourly

285 2 m temperature from ERA5-Land data (Muñoz Sabater, 2019). Both were aggregated to the 0.5° GOME-2A SIF grid. The summers of 2007 to 2012 in Shaanxi and surrounding provinces are characterized by soil moisture values (45–55 %) that are generally good for plant growth, showed a slight increase over time (1 % yr^{-1}), and by relatively stable (average) maximum temperatures. The summer of 2010 was somewhat of an exception with maximum temperature more than 1 °C below the multi-annual mean, which we interpret as indicating lower radiation levels. Overall, we expect that interannual variability in

290 climate factors has favoured forest growth between 2007 and 2012 in both the reforested and deforested areas in line with previous studies (e.g. Zhang et al., 2022). Overall conditions for vegetation growth appear more favourable in cells where reforestation occurred as maximum temperatures were more moderate (23 °C) and soil moisture was higher (53 %) in the cells with reforestation than in cells with deforestation.

4.2 Interpretation of temporal variability in SIF

295 We constructed a simple model that expresses the local year-to-year variability in summertime SIF as a linear combination of soil moisture (S) (in %), maximum temperature (T) (in °C), averaged over spring to summertime (March–August), and the total forest coverage (A) (in km^2) – Eq. (3). The selection of this model is motivated by three factors: (i) soil moisture promotes the thriving of vegetation by enhancing the water availability, (ii) increasing temperature stimulates vegetation activity until an optimal temperature is reached (Gao et al., 2019), and is a proxy for photosynthetic active radiation, and (iii) total photosyn-

300 thetic carbon uptake increases with increasing vegetation cover. Note that the climate parameters are averaged over the spring and summer period (March–Aug) to account for the concurrent and lagged effects on the vegetation activity over summer (e.g. Sun et al. (2021)).

We use a multivariate least-squares regression to optimize the combined fit coefficients that best explain the observed SIF over the reforested and deforested cells. Modelled SIF as a function of year (between 2007 and 2012), F_{mod} (t), is expressed

305 as:

$$F_{\mathrm{mod}}(t) = \alpha S(t) + \beta T(t) + \gamma A(t) + \delta \tag{3}$$

where α, β, γ and δ represent the coefficients that minimize the discrepancies (ϵ) between F_{mod} (t) and the observed GOME-2A time series F_{obs} (t). To ensure sufficient statistics, we pooled the time series of SIF (n=6) from all 50 selected cells, resulting in a single, cell-ensemble fit. Overall, the modelled variability in SIF matches the measured variability reasonably well (R^2=0.57,

310 n=300). Figure 8a shows the correlation between the observed (F_{obs}) and modelled SIF (F_{mod}) over all cells.
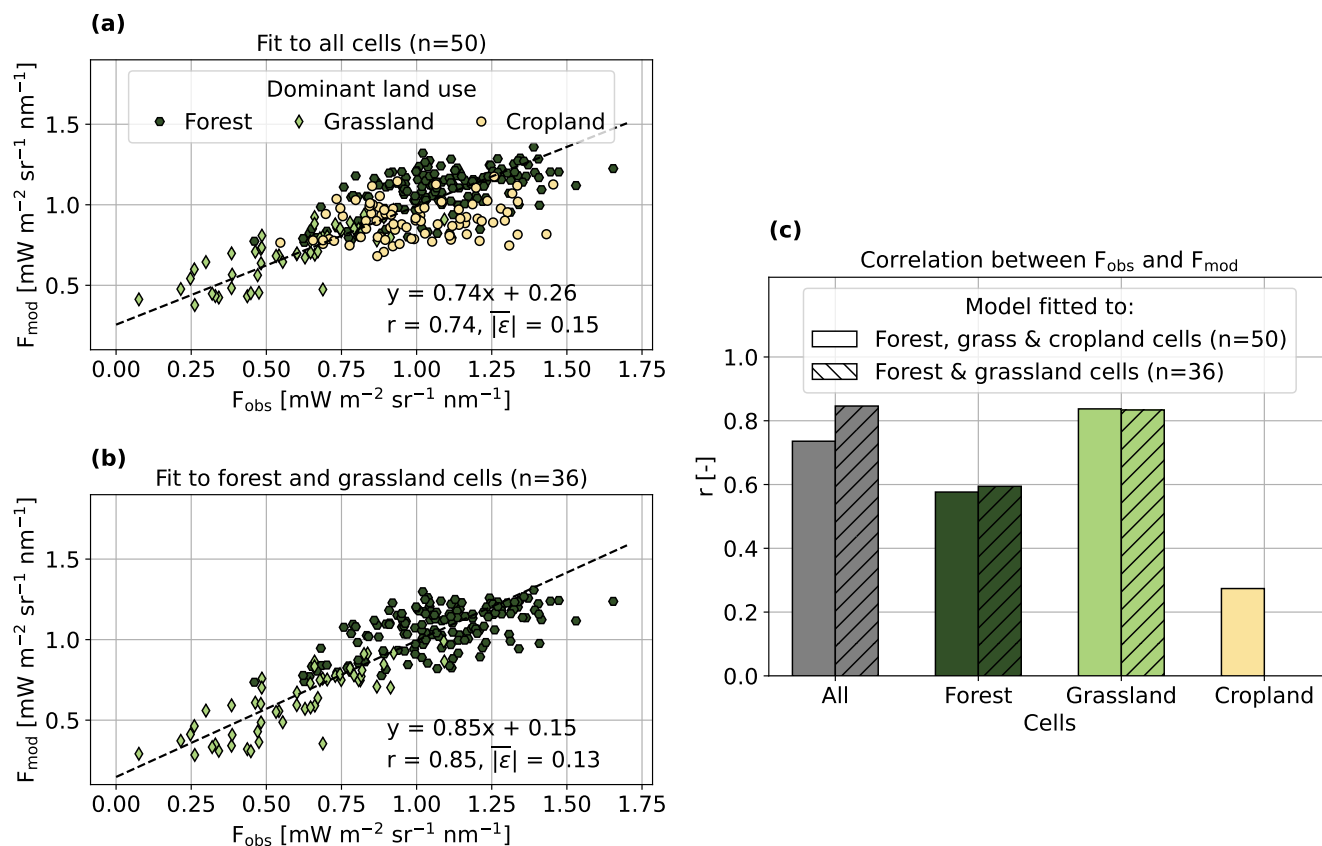
Figure 8. Results from the regression model in Eq. (3) fitted to (a) all cells (n=50) and (b) exclusively to forest and grassland cells (n=36). (c) Shows the correlation between observed (F_{obs}) and modelled (F_{mod}) SIF for each dominant land type and for both fits.

However, the model's performance varied by land use type across the region (Fig. 8c). Notably, it demonstrated good agreement between observed and modelled values for cells dominated by grassland (r=0.84) or forest cover (r=0.58), but struggled with representing the dynamics in cropland cells (r=0.27). This suggests distinct differences in the underlying dynamics and complexities in converting cropland areas into forest, which previous studies reported to croplands often being located in dryer

315 areas with less forest cover to begin with, reducing the vigour with which vegetation increases in response to reforestation (Qu et al., 2020).

We therefore exclusively fitted our final model to data from the 36 cells dominated by grassland or forest cover (n=216) (Fig. 8b and c). By excluding cropland cells, the fit significantly improved, evident from the higher R^2 of 0.72. The improved correlation between the observed and modelled SIF suggests that the model better captures the underlying dynamics. Note that

320 our model is specific to the fitted area and period. Next, to evaluate the explanatory power of including forest coverage in our model, we constructed an alternative model that solely fits the first two terms on the right-hand side of Eq. (3), i.e. the climate parameters to the observed summertime SIF. Doing so allows us to compute the R^2 adjusted of our model (Eq. (3)) and the

alternate model to enable fair comparison between the models containing three and two predictors, respectively. The alternate

model had an adjusted R^2 of 0.66. With the inclusion of forest cover data, the model's performance improved, achieving an ad-

325   justed R^2 adjusted of 0.71 – suggesting added value of including changed forest coverage in conjunction to climate variability

in the model.

Table 1. Regression results of model fitted to GOME-2A summertime SIF temporal variability over reforested and deforested cells with as dominant land use of grassland or forest (*n*=36). The model was fitted to data spanning between 2007 and 2012. Uncertainty is given in standard error (SE).

Predictor		Fit coefficients		Average *	Average change *
		Value $\times 10^{-3}$	Scaled value	2007	2007-2012
Soil moisture	α	18.65±2.31 mW m^{-2} sr^{-1} nm^{-1} %$^{-1}$	0.55±0.06	51.5±1.5 %	+4.8±0.6 %
Max. temp.	β	35.98±6.86 mW m^{-2} sr^{-1} nm^{-1} °C^{-1}	0.21±0.04	23.0±0.3 °C	-0.4±0.1 °C
Forest cover	γ	0.15±0.02 mW m^{-2} sr^{-1} nm^{-1} km^{-2}	0.38±0.06	1290.7±129.8 km^2	+96.9±6.9 km^2

R^2 = 0.72

* Over reforested cells (=31)

The model's fit coefficients, presented in Table 1, demonstrate, as hypothesized, that increases in the predictors positively

influence SIF. Soil moisture and forest cover variability explain most of the variability in GOME-2A SIF, as indicated by the

330   scaled values of the fit coefficients (that consider predictor standard deviations). This is also expected given the relatively strong

increases in soil moisture (+5 %) and in forest cover (+97 km^2) compared to the modest changes in maximum temperature over

the provinces from 2007 and 2012. The effect of changes in soil moisture cannot be disentangled from the effect of changes in

forest cover on vegetation activity. They are likely occurring in tandem, because soils in regions with increased tree cover tend

to hold on better to their soil moisture. We also tested a model including an additional (fourth) interaction term between soil

335   moisture and reforestation, but this did not lead to an improved R^2 adjusted between modelled and observed SIF. We conclude

that vegetation activity following reforestation efforts increases most over temperate areas in northern China classified as

grassland and forest, with relatively high soil moisture to begin with. On average, these areas show high covariance between

changes in soil moisture and changes in forest cover, indicating that both factors explain the increase in summertime SIF.

5   Conclusions and Discussion

340   Satellite-based solar-induced fluorescence (SIF) observations, a measure of plant photosynthesis, emerge as a promising tool

to track changes in carbon uptake in response to land use change. In this study we demonstrated that TROPOMI SIF captures

sharp local reductions in vegetation activity —and thus carbon uptake— in the aftermath of a large forest fire in southeastern

Australia, the Nunnett-Timbarra River fire, in 2019, but also that TROPOMI SIF tracks rapid recovery of vegetation activity in

the affected area. By careful cross-evaluation of TROPOMI SIF with coinciding tower- and model-based estimates of global

345 primary productivity (GPP), we estimate that the Nunnett-Timbarra River fire caused a reduction of SIF by, on average, 0.2 mW m^{-2} sr^{-1} nm^{-1} corresponding to 130-200 GgC that would otherwise have been stored by the 210 km^2 Eucalypt Forest if no fire had occurred in the first eight post-fire months. This shows that TROPOMI SIF is well-capable of monitoring sudden changes in vegetation activity at a scale of some 20×10 km^2 and this predicts excellent potential for the Fluorescence Explorer (FLEX, to be launched in 2025) to monitor changes in carbon uptake from land management techniques which often occur at

350 much smaller spatial scales than the Nunnett-Timbarra River fire.

We also found increases in GOME-2A SIF of 0.1–0.2 mW m^{-2} sr^{-1} nm^{-1} over the provinces of Shaanxi, Gansu, Sichuan, and Chonqing in northern China in the period 2007–2012, when China effectuated a large-scale reforestation program aimed at reversing desertification. In contrast, in areas where deforestation occurred, GOME-2A SIF showed a reduction in SIF of 0.1 m^{-2} sr^{-1} nm^{-1} over the same period. That it is possible with GOME-2A SIF to track reforestation (and deforestation) is

355 supported by independent and co-sampled measurements from MODIS NIRv and by the FluxSat model product over the same areas also indicating increased (and decreased) vegetation activity. The relatively course-scale GOME-2A SIF measurements (40×80 km^2) indicate that vegetation activity increased the most in regions with relatively high soil moisture content and substantial reforestation as diagnosed by the China Land Cover dataset. This suggests that reforestation is effective in enhancing carbon storage in the relatively wet and temperate regions of northern China, but less so in the sub-tropical parts of the

360 provinces, which are dryer and hotter. Interpreting the observed temporal variability in GOME-2A SIF from 2007 to 2012 with a simple model that accounts for simultaneous spatio-temporal changes in soil moisture, maximum temperature, and in forest cover, we found that the observed SIF-changes in northern China can be explained well (R^2=0.72) over areas with forest and grassland that underwent reforestation. Reforestation efforts, in step with soil moisture increases, appear to be driving the observed increase in SIF. This implies that the impact of reforestation on increases in SIF should be interpreted in the context

365 of simultaneous increases soil moisture.

Satellite-based SIF observations emerge as a promising method to facilitate the tracking of carbon uptake in response to land use change. Through the analysis of two distinct cases of forest cover change, we demonstrated the applicability of SIF as monitoring tool, in combination with satellite-data that maps the land use change. The supporting data facilitates the pinpointing of SIF cells aligned with land cover changes. Our comparative approach revealed distinct changes in SIF dynamics

370 related to shifts in forest coverage. This underscores the capability of SIF to capture the impact of land cover change, whether driven by distinct abrupt events or gradual transitions, on regional vegetation activity.

Our work underscores that satellite measurements of SIF are useful to monitor changes in carbon uptake following land use change as long as the spatial and temporal scales at which these occur are sharply demarcated. In this study, the availability of high-resolution MODIS burned area (pixel size 1×1 km^2) and TROPOMI SIF (pixel size 7×3.5 km^2) made it possible to

375 detect sharp changes in vegetation activity following a devastating fire over a relatively large area. It is also possible to attribute observed increases in GOME-2A SIF to changes that occur much slower and on an even much larger spatial scale, such as the reforestation efforts in norther China, but this requires the careful selection and co-sampling of explanatory biogeographical data, such as information on soil moisture, temperature, and forest cover.

Code availability. The code to co-sample spatio-temporal changes in SIF and in supporting data is available upon request from the first
380 author.

Data availability. All data used in this study are publicly available. The GOME-2 SIF data are provided by KNMI in the framework of
the EUMETSAT Satellite Application Facility on Atmospheric Composition Monitoring (AC SAF). KNMI GOME-2A SIF data can be
downloaded from www.temis.nl.

Appendix A: Relationships between TROPOMI SIF and GPP over Eucalyptus forest

385 The SIF–GPP relationship over Eucalyptus forest was obtained using TROPOMI SIF observations and GPP estimates from the
eddy-covariance flux site in Tumbarumba (AU-TUM: 35.66° N, 148.15° E). We also used FluxSat GPP to infer an alternative
SIF–GPP relationship over the Eucalyptus forest at Tumbarumba. We inferred the empirical relationships from fitting instan-
taneous (TROPOMI overpass-time) SIF and daily-aggregated GPP data. In contrast to strategies using daily-corrected SIF for
the analysis (Zhang et al., 2018; Turner et al., 2021), we chose here to use instantaneous SIF because the SIF signal in our
390 region of interest is of low magnitude and the daily-correction would decrease the magnitude even further. Furthermore, the
use of instantaneous SIF observations avoid simplified assumptions regarding the scaling of SIF with the amount of sunlight
available for photosynthesis.

Reduced major axis regression (RMA) was used to obtain the empirical relationships between SIF and GPP. The RMA
regression accounts for uncertainty in both the SIF observations and GPP data. The use of a linear regression is reasonable
395 following the implied linear relation of SIF–GPP during most daily conditions (Porcar-Castell et al., 2014) as well as the
enforced linearity due to integration of the over the canopy (Magney et al., 2020). The regression analysis of SIF vs GPP
clearly indicates the presence an intercept for the best fit (Fig. A2). Furthermore, the top-of-canopy SIF depends on the escape
ratio of the photons from the canopy and, theoretically, space-based SIF could approach to zero even if GPP is not 0.

Table A1. SIF–GPP relations using instantenous TROPOMI SIF and daily GPP from the OzFlux dataset and FluxSat over the Tumbarumba
flux tower. The OzFlux data represents the GPP estimates from the Tumbarumba tower. SIF is in units of mW m^{-2} sr^{-1} nm^{-1} and GPP in
gC m^{-2} day^{-1}. SIF and GPP data have been co-sampled such that observations correspond to the same dates. To account for the smaller
footprint of the eddy-covariance measurements, typically in the range of 100–1000 m, we selected TROPOMI SIF observations within a
distance of 7 km (1 pixel) from the Tumbarumba site. The FluxSat GPP cells were selected to match the coverage of the TROPOMI SIF
observations.

GPP source	SIF–GPP		SIF–GPP, no intercept
OzFlux	$r = 0.91$	GPP = 11.10 SIF + 0.81	GPP = 12.19 SIF
FluxSat	$r = 0.94$	GPP = 5.56 SIF + 1.37	GPP = 7.40 SIF
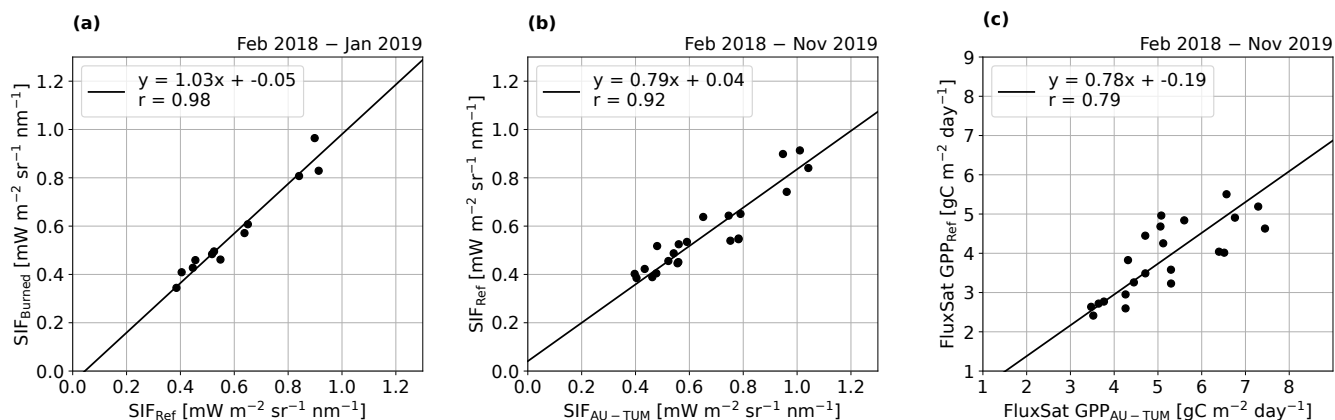
Figure A1. Correlation in the period February 2018 – January 2019 between (a) TROPOMI SIF over the reference area and area that would later burn down, and correlation in the period February 2018 – November 2019 between (b) TROPOMI SIF over the Tumbarumba flux tower site (AU-TUM) and TROPOMI SIF over the reference area. Subplot (c) shows the correlation between FluxSat GPP over the Tumbarumba site and the reference area.
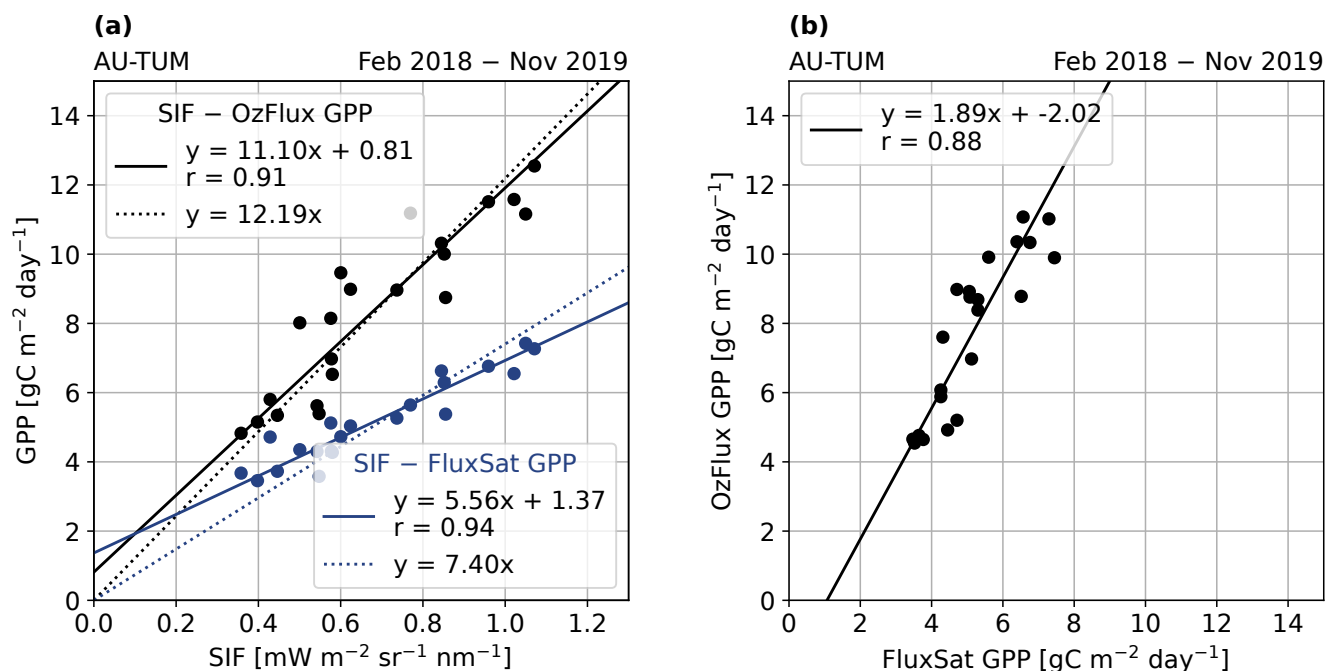
Figure A2. Correlation between (a) the TROPOMI SIF and daily GPP with flux tower and FluxSat GPP in black and blue, respectively, at the Tumbarumba Flux tower site (AU-TUM) and (b) monthly aggregated daily GPP versus the monthly averaged GPP where accounted days match SIF observations (collocated) at AU-TUM.
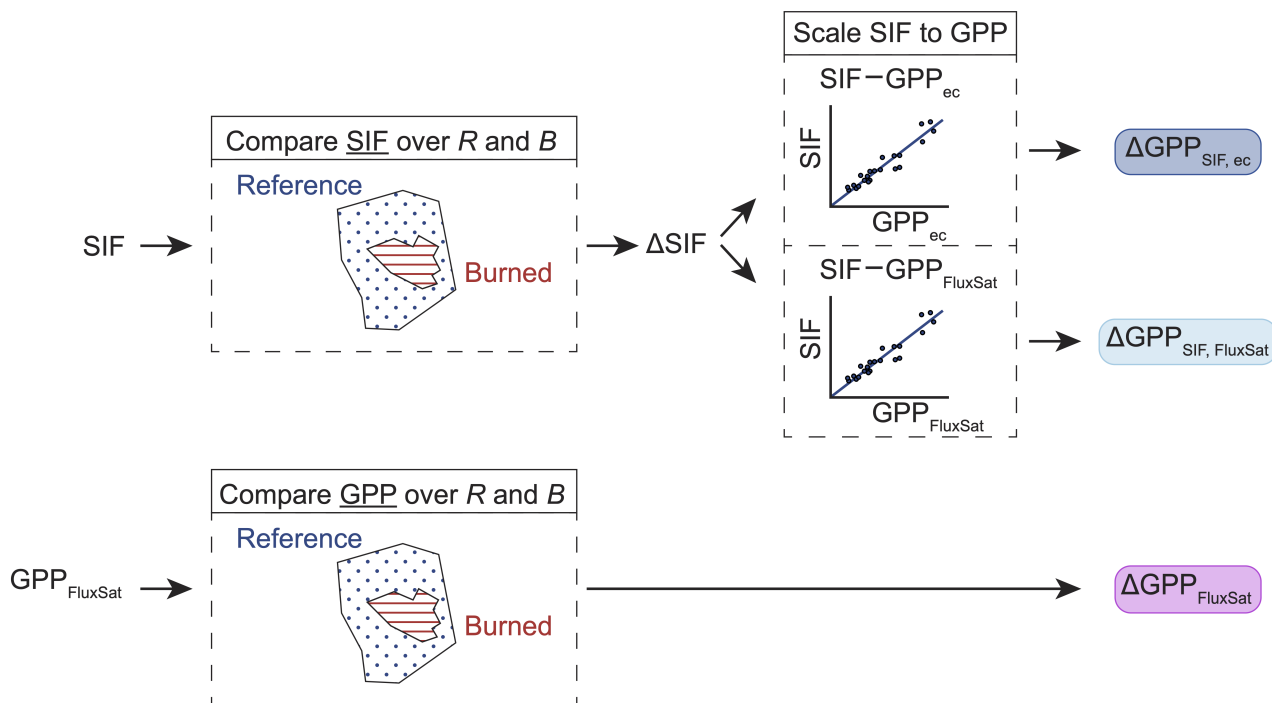
Figure A3. Outline of the derivation of the loss in GPP over the burned area: SIF-based GPPs, inferred from SIF–GPP relationship using eddy covariance data from the Tumbarumba OzFlux site and FluxSat GPP, and GPP directly from FluxSat GPP.

Appendix B: Trend correction GOME-2A SIF over northern China

To assess the stability of GOME-2A SIF (SIFTER v2) over north-central China, we used SIF time series over the nearby Gobi Desert (95.5–105.5° E, 40.5–44° N). Figure B1 shows the monthly GOME-2A SIF over the Gobi Desert from 2007 to 2018. The colors indicate the respective level-1 processor version over time. Over the early period, 2007–2013, a gradual trend is noticed from around 2011. The striking positive shift in baseline SIF levels from July 2013 relates to the smaller range in viewing zenith angle (< 35°) following the swath reduction on 15 July 2013. From June 2014, the higher baseline trend appears to be broken for a period of 5-6 months. Figure B2 shows a similar structural break occurring over Sahara and 30–40° N ocean SIF pixels. The timing of the sudden drop in SIF signal coincides with the change of level-1 processor version 5.3 to 6.0 (18-05-2014) (Fig. B1), and thus suggests a significant influence of these changes on SIF. For our analysis, we solely use the GOME-2A data from the pre-2013 period to control the record's stability. Reprocessing the SIFTER v2 SIF data using level-1 data based on the recent processor version 6.3 that covers the entire data record will eliminate the uncertainty related to level-1 processor changes throughout the data record.
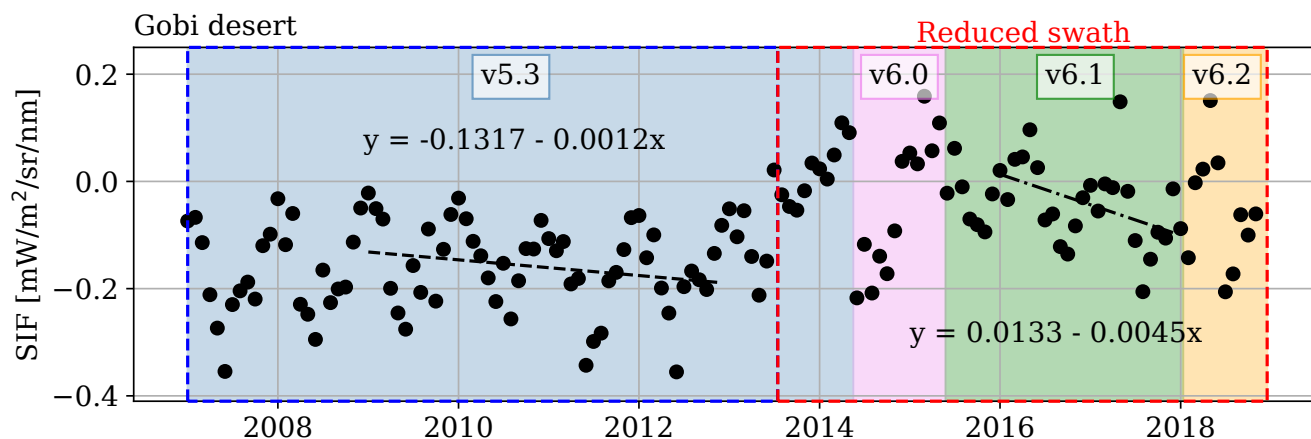
Figure B1. Monthly SIF retrieved from GOME-2A measurements as a function of time over the Gobi Desert (95.5–105.5 °E, 40.5–44 °N). The colored blocks indicate the used level-1 processor version (v5.3, v6.0, v6.1 and v6.2) over time. The record can be seen as coming from two different sensors, with the early and late period differentiated by timing of the swath reduction at 15-06-2013. The early period and late period are, respectively, indicated by the blue and red dotted blocks.
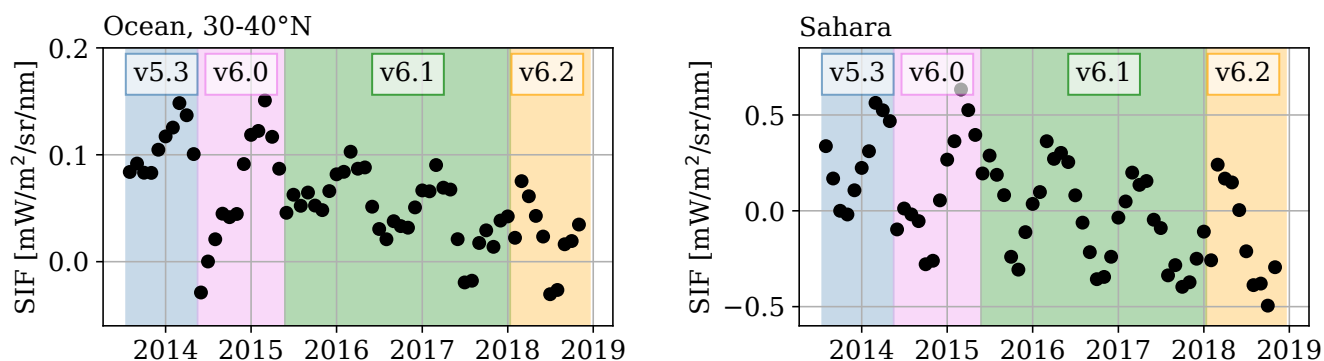
Figure B2. Monthly SIF retrieved from GOME-2A measurements as a function of time over the ocean (30 to 40° N) and the Sahara Desert (-8° W to 29° E, 15 to 30° N) over the late sensor period after the swath reduction at 15-06-2013. The colored blocks indicate the used level-1 processor version (v5.3, v6.0, v6.1 and v6.2) over time.

To correct for the noticed gradual trend over the early period, a multiplicative correction factor is applied. Gerlein-Safdi et al. (2020) used latitudinal average SIF to obtain multiplicative correction factors to correct for GOME-2A SIF over northern China (30–40° N). However, the SIF dynamics over the 30–40° N latitudinal band differ strongly over longitude: with higher SIF values over the west and lower over the east (e.g. north-central China). Furthermore, SIF cells that cover vegetational areas could represent the imprint of climatic variation and thus cause biases within the correction factor. The average of SIF over the

Gobi desert (free of vegetation) area is expected to stay stable over time and not to be influenced by factors such as climatic fluctuation.

The year-specific correction factor is determined over the Gobi Desert area and corrects for the deviation in yearly SIF at year t with respect to the yearly SIF average over 2007 to 2012 the period of the reference spectra used in the SIFTER v2
420   retrieval. Therefore, the corrected SIF, $F_{(C,i)}$ (t), over cell i and year t is calculated as:

$$F_{C,i}(t) = F_i(t)\frac{\overline{F_{Gobi}}}{F_{Gobi\,('07-'12)}(t)} \tag{B1}$$

where $\overline{F_{Gobi('07-'12)}}$ represents the 2007-2012 average of SIF over the Gobi Desert and F_{Gobi} (t) the averaged SIF over the Gobi Desert in year t. Yearly SIF over the Gobi Desert is used to determine the correction to limit the uncertainty coming from the low signal levels over the area. Correction values deviate between 0.85 and 1.12. Figure B3 shows the correlation between
425   between FluxSat GPP with uncorrected and corrected GOME-2A SIF over our study region in China.
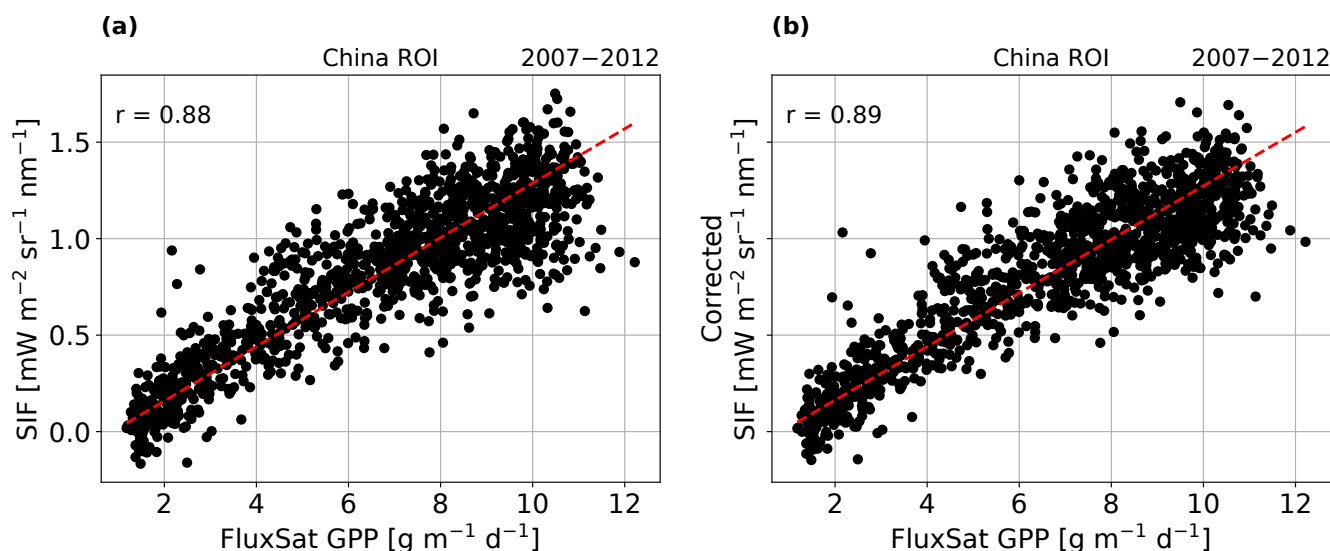
Figure B3. (a) Correlation between FluxSat GPP and SIF and (b) correlation between FluxSat GPP and corrected SIF over the China ROI area (104.5°–112° E, 31°–38° N). The data points present SIF and GPP between 2007 and 2012 and over the summer period (June–August).

Author contributions. JA and KFB designed the study and led the writing. JA performed the data analysis. PS contributed to the interpretation of the results and to all versions of the manuscript and figures. GK provided and conducted the analysis of the MODIS NIRv data over northern China. PK and CF contributed to the interpretation of the results of TROPOMI SIF over Australia. WW and JS provided the OzFlux data and contributed to the validity of SIF–GPP over Australia. All co-authors reviewed the paper.

430 *Competing interests.* The contact author has declared that none of the authors has any competing interests.

Acknowledgements. This work received funding from the European Union's Horizon2020 research and innovations program under grant agreement No 869367 (EU LANDMARC project), and from EUMETSAT's Atmospheric Composition Satellite Application Facility (AC-SAF). We acknowledge the free use of SIFTER Sun-Induced Fluorescence data from the (GOME-2A) sensor from www.temis.nl. Furthermore, we would like to thank LANDMARC-colleagues Dr. Markus Donat from Barcelona Supercomputing Center (BSC) for the discussion
435 on intercomparison of SIF with climate variables, and Dr. Moritz Laub from ETH Zürich for the discussion of the wildfire impact on the carbon cycle perturbation.

References

Ač, A., Malenovský, Z., Olejníčková, J., Gallé, A., Rascher, U., and Mohammed, G.: Meta-analysis assessing potential of steady-state chlorophyll fluorescence for remote sensing detection of plant water, temperature and nitrogen stress, Remote Sensing of Environment, 168, 420–436, https://doi.org/10.1016/j.rse.2015.07.022, 2015.

Bacour, C., Maignan, F., MacBean, N., Porcar-Castell, A., Flexas, J., Frankenberg, C., Peylin, P., Chevallier, F., Vuichard, N., and Bastrikov, V.: Improving Estimates of Gross Primary Productivity by Assimilating Solar-Induced Fluorescence Satellite Retrievals in a Terrestrial Biosphere Model Using a Process-Based SIF Model, Journal of Geophysical Research: Biogeosciences, 124, 3281–3306, https://doi.org/10.1029/2019JG005040, 2019.

Bowman, D. M., Williamson, G. J., Price, O. F., Ndalila, M. N., and Bradstock, R. A.: Australian forests, megafires and the risk of dwindling carbon stocks, Plant Cell and Environment, 44, 347–355, https://doi.org/10.1111/pce.13916, 2021.

Brook, B. W., Ellis, E. C., Perring, M. P., Mackay, A. W., and Blomqvist, L.: Does the terrestrial biosphere have planetary tipping points?, Trends in Ecology and Evolution, 28, 396–401, https://doi.org/10.1016/j.tree.2013.01.016, 2013.

Byrne, B., Liu, J., Yin, Y., and Bowman, K.: The carbon cycle of southeast Australia during 2019-2020 : Drought , fires and subsequent recovery This manuscript is a preprint and has been submitted for publication as a, 2021.

Cao, S., Chen, L., and Yu, X.: Impact of China's Grain for Green Project on the landscape of vulnerable arid and semi-arid agricultural regions: A case study in northern Shaanxi Province, Journal of Applied Ecology, 46, 536–543, https://doi.org/10.1111/j.1365-2664.2008.01605.x, 2009.

Chu, X. X., Zhan, J., Li, Z., Zhang, F., and Qi, W.: Assessment on forest carbon sequestration in the Three-North Shelterbelt Program region, China, Journal of Cleaner Production, 215, 382–389, https://doi.org/10.1016/j.jclepro.2018.12.296, 2019.

Chungu, D., Ng'andwe, P., Mubanga, H., and Chileshe, F.: Fire alters the availability of soil nutrients and accelerates growth of Eucalyptus grandis in Zambia, Journal of Forestry Research, 31, 1637–1645, https://doi.org/10.1007/s11676-019-00977-y, 2020.

Dechant, B., Ryu, Y., Badgley, G., Zeng, Y., Berry, J. A., Zhang, Y., Goulas, Y., Li, Z., Zhang, Q., Kang, M., Li, J., and Moya, I.: Canopy structure explains the relationship between photosynthesis and sun-induced chlorophyll fluorescence in crops, Remote Sensing of Environment, 241, https://doi.org/10.1016/j.rse.2020.111733, 2020.

Delang, C. O. and Yuan, Z.: China's Grain for Green Program, https://doi.org/10.1007/978-3-319-11505-4, 2015.

Dorigo, W., Preimesberger, W., Reimer, C., Van der Schalie, R., Pasik, A., De Jeu, R., and Paulik, C.: Soil moisture gridded data from 1978 to present, v201912.0.0., https://cds.climate.copernicus.eu/cdsapp{#}!/dataset/satellite-soil-moisture?tab=overview, 2019.

Doughty, R., Köhler, P., Frankenberg, C., Magney, T. S., Xiao, X., Qin, Y., Wu, X., and Moore, B.: TROPOMI reveals dry-season increase of solar-induced chlorophyll fluorescence in the Amazon forest, Proceedings of the National Academy of Sciences of the United States of America, 116, 22 393–22 398, https://doi.org/10.1073/pnas.1908157116, 2019.

Drusch, M., Moreno, J., Del Bello, U., Franco, R., Goulas, Y., Huth, A., Kraft, S., Middleton, E. M., Miglietta, F., Mohammed, G., Nedbal, L., Rascher, U., Schüttemeyer, D., and Verhoef, W.: The FLuorescence EXplorer Mission Concept—ESA's Earth Explorer 8, IEEE Transactions on Geoscience and Remote Sensing, 55, 1273–1284, https://doi.org/10.1109/TGRS.2016.2621820, 2016.

Duffy, K. A., Schwalm, C. R., Arcus, V. L., Koch, G. W., Liang, L. L., and Schipper, L. A.: How close are we to the temperature tipping point of the terrestrial biosphere?, Science Advances, 7, 1–9, https://doi.org/10.1126/sciadv.aay1052, 2021.

Fancourt, M., Ziv, G., Boersma, K. F., Tavares, J., Wang, Y., and Galbraith, D.: Background climate conditions regulated the photosynthetic response of Amazon forests to the 2015/2016 El Nino-Southern Oscillation event, Communications Earth and Environment, 3, 1–9, https://doi.org/10.1038/s43247-022-00533-3, 2022.

475 Frankenberg, C. and Berry, J.: Solar induced chlorophyll fluorescence: Origins, relation to photosynthesis and retrieval, 1986, Elsevier, https://doi.org/10.1016/B978-0-12-409548-9.10632-3, 2017.

Frankenberg, C., Fisher, J. B., Worden, J., Badgley, G., Saatchi, S. S., Lee, J. E., Toon, G. C., Butz, A., Jung, M., Kuze, A., and Yokota, T.: New global observations of the terrestrial carbon cycle from GOSAT: Patterns of plant fluorescence with gross primary productivity, Geophysical Research Letters, 38, 1–6, https://doi.org/10.1029/2011GL048738, 2011.

480 Friedlingstein, P., O'Sullivan, M., Jones, M. W., Andrew, R. M., Hauck, J., Olsen, A., Peters, G. P., Peters, W., Pongratz, J., Sitch, S., Le Quéré, C., Canadell, J. G., Ciais, P., Jackson, R. B., Alin, S., Aragão, L. E. O. C., Arneth, A., Arora, V., Bates, N. R., Becker, M., Benoit-Cattin, A., Bittig, H. C., Bopp, L., Bultan, S., Chandra, N., Chevallier, F., Chini, L. P., Evans, W., Florentie, L., Forster, P. M., Gasser, T., Gehlen, M., Gilfillan, D., Gkritzalis, T., Gregor, L., Gruber, N., Harris, I., Hartung, K., Haverd, V., Houghton, R. A., Ilyina, T., Jain, A. K., Joetzjer, E., Kadono, K., Kato, E., Kitidis, V., Korsbakken, J. I., Landschützer, P., Lefèvre, N., Lenton, A., Lienert, S., 485 Liu, Z., Lombardozzi, D., Marland, G., Metzl, N., Munro, D. R., Nabel, J. E. M. S., Nakaoka, S.-I., Niwa, Y., O'Brien, K., Ono, T., Palmer, P. I., Pierrot, D., Poulter, B., Resplandy, L., Robertson, E., Rödenbeck, C., Schwinger, J., Séférian, R., Skjelvan, I., Smith, A. J. P., Sutton, A. J., Tanhua, T., Tans, P. P., Tian, H., Tilbrook, B., van der Werf, G., Vuichard, N., Walker, A. P., Wanninkhof, R., Watson, A. J., Willis, D., Wiltshire, A. J., Yuan, W., Yue, X., and Zaehle, S.: Global Carbon Budget 2020, Earth System Science Data, 12, 3269–3340, https://doi.org/10.5194/essd-12-3269-2020, 2020.

490 Gao, J., Jiao, K., and Wu, S.: Investigating the spatially heterogeneous relationships between climate factors and NDVI in China during 1982 to 2013, Journal of Geographical Sciences, 29, 1597–1609, https://doi.org/10.1007/s11442-019-1682-2, 2019.

Gerlein-Safdi, C., Keppel-Aleks, G., Wang, F., Frolking, S., and Mauzerall, D. L.: Satellite Monitoring of Natural Reforestation Efforts in China's Drylands, One Earth, 2, 98–108, https://doi.org/10.1016/j.oneear.2019.12.015, 2020.

Getachew Mengistu, A., Mengistu Tsidu, G., Koren, G., Kooreman, M. L., Folkert Boersma, K., Tagesson, T., Ardö, J., Nouvellon, Y., and 495 Peters, W.: Sun-induced fluorescence and near-infrared reflectance of vegetation track the seasonal dynamics of gross primary production over Africa, Biogeosciences, 18, 2843–2857, https://doi.org/10.5194/bg-18-2843-2021, 2021.

Giglio, L., Justice, C., Boschetti, L., and Roy, D.: MCD64A1 MODIS/Terra+Aqua Burned Area Monthly L3 Global 500m SIN Grid V006 [Data set]. NASA EOSDIS Land Processes DAAC., https://doi.org/https://doi.org/10.5067/MODIS/MCD64A1.006, 2015.

Guanter, L., Zhang, Y., Jung, M., Joiner, J., Voigt, M., Berry, J. A., Frankenberg, C., Huete, A. R., Zarco-Tejada, P., Lee, J. E., Moran, 500 M. S., Ponce-Campos, G., Beer, C., Camps-Valls, G., Buchmann, N., Gianelle, D., Klumpp, K., Cescatti, A., Baker, J. M., and Griffis, T. J.: Global and time-resolved monitoring of crop photosynthesis with chlorophyll fluorescence, Proceedings of the National Academy of Sciences of the United States of America, 111, https://doi.org/10.1073/pnas.1320008111, 2014.

Guo, M., Li, J., Yu, F., Yin, S., Huang, S., and Wen, L.: Estimation of post-fire vegetation recovery in boreal forests using solar-induced chlorophyll fluorescence (SIF) data, International Journal of Wildland Fire, 30, 365–377, https://doi.org/10.1071/WF20162, 2021.

505 Harper, A. B., Powell, T., Cox, P. M., House, J., Huntingford, C., Lenton, T. M., Sitch, S., Burke, E., Chadburn, S. E., Collins, W. J., Comyn-Platt, E., Daioglou, V., Doelman, J. C., Hayman, G., Robertson, E., van Vuuren, D., Wiltshire, A., Webber, C. P., Bastos, A., Boysen, L., Ciais, P., Devaraju, N., Jain, A. K., Krause, A., Poulter, B., and Shu, S.: Land-use emissions play a critical role in land-based mitigation for Paris climate targets, Nature Communications, 9, https://doi.org/10.1038/s41467-018-05340-z, 2018.

Huntzinger, D. N., Michalak, A. M., Schwalm, C., Ciais, P., King, A. W., Fang, Y., Schaefer, K., Wei, Y., Cook, R. B., Fisher, J. B., Hayes, D., Huang, M., Ito, A., Jain, A. K., Lei, H., Lu, C., Maignan, F., Mao, J., Parazoo, N., Peng, S., Poulter, B., Ricciuto, D., Shi, X., Tian, H., Wang, W., Zeng, N., and Zhao, F.: Uncertainty in the response of terrestrial carbon sink to environmental drivers undermines carbon-climate feedback predictions, Scientific Reports, 7, 1–8, https://doi.org/10.1038/s41598-017-03818-2, 2017.

Isaac, P., Cleverly, J., McHugh, I., Van Gorsel, E., Ewenz, C., and Beringer, J.: OzFlux data: Network integration from collection to curation, Biogeosciences, 14, 2903–2928, https://doi.org/10.5194/bg-14-2903-2017, 2017.

Joiner, J., Yoshida, Y., Vasilkov, A. P., Yoshida, Y., Corp, L. A., and Middleton, E. M.: First observations of global and seasonal terrestrial chlorophyll fluorescence from space, Biogeosciences, 8, 637–651, https://doi.org/10.5194/bg-8-637-2011, 2011.

Joiner, J., Guanter, L., Lindstrot, R., Voigt, M., Vasilkov, A. P., Middleton, E. M., Huemmrich, K. F., Yoshida, Y., and Frankenberg, C.: Global monitoring of terrestrial chlorophyll fluorescence from moderate-spectral-resolution near-infrared satellite measurements: methodology, simulations, and application to GOME-2, Atmospheric Measurement Techniques, 6, 2803–2823, https://doi.org/10.5194/amt-6-2803-2013, 2013.

Joiner, J., Yoshida, Y., Guanter, L., and Middleton, E. M.: New methods for the retrieval of chlorophyll red fluorescence from hyperspectral satellite instruments: Simulations and application to GOME-2 and SCIAMACHY, Atmospheric Measurement Techniques, 9, 3939–3967, https://doi.org/10.5194/amt-9-3939-2016, 2016.

Joiner, J., Yoshida, Y., Zhang, Y., Duveiller, G., Jung, M., Lyapustin, A., Wang, Y., and Tucker, C. J.: Estimation of terrestrial global gross primary production (GPP) with satellite data-driven models and eddy covariance flux data, Remote Sensing, 10, 1–38, https://doi.org/10.3390/rs10091346, 2018.

Köhler, P., Frankenberg, C., Magney, T. S., Guanter, L., Joiner, J., and Landgraf, J.: Global Retrievals of Solar-Induced Chlorophyll Fluorescence With TROPOMI: First Results and Intersensor Comparison to OCO-2, Geophysical Research Letters, 45, 10,456–10,463, https://doi.org/10.1029/2018GL079031, 2018.

Kong, Z. H., Stringer, L. C., Paavola, J., and Lu, Q.: Situating China in the global effort to combat desertification, Land, 10, 1–22, https://doi.org/10.3390/land10070702, 2021.

Kooreman, M. L., Boersma, K. F., van Schaik, E., van Versendaal, R., Cacciari, A., and Tuinder, O. N. E.: SIFTER sun-induced vegetation fluorescence data from GOME-2A (Version 2.0) [Data set], Royal Netherlands Meteorological Institute (KNMI), https://doi.org/10.21944/gome2a-sifter-v2-sun-induced-fluorescence, 2020.

Li, S., Yang, S., Liu, X., Liu, Y., and Shi, M.: NDVI-based analysis on the influence of climate change and human activities on vegetation restoration in the shaanxi-gansu-ningxia region, central China, Remote Sensing, 7, 11 163–11 182, https://doi.org/10.3390/rs70911163, 2015.

Li, X. and Xiao, J.: TROPOMI observations allow for robust exploration of the relationship between solar-induced chlorophyll fluorescence and terrestrial gross primary production, Remote Sensing of Environment, 268, https://doi.org/10.1016/j.rse.2021.112748, 2022.

Lin, X., Niu, J., Berndtsson, R., Yu, X., Zhang, L., and Chen, X.: Ndvi dynamics and its response to climate change and reforestation in Northern China, Remote Sensing, 12, 1–15, https://doi.org/10.3390/rs12244138, 2020.

Lindenmayer, D. B. and Taylor, C.: New spatial analyses of Australian wildfires highlight the need for new fire, resource, and conservation policies, Proceedings of the National Academy of Sciences of the United States of America, 117, 12 481–12 485, https://doi.org/10.1073/pnas.2002269117, 2020.

Liu, L., Guan, L., and Liu, X.: Directly estimating diurnal changes in GPP for C3 and C4 crops using far-red sun-induced chlorophyll fluorescence, Agricultural and Forest Meteorology, 232, 1–9, https://doi.org/10.1016/j.agrformet.2016.06.014, 2017.

Lymburner, L., Tan, P., McIntyre, A., Tankappan, M., and Sixsmith, J.: Dynamic Land Cover Dataset Version 2.1., 2015.

Madani, N., Parazoo, N. C., Kimball, J. S., Reichle, R. H., Chatterjee, A., Watts, J. D., Saatchi, S., Liu, Z., Endsley, A., Tagesson, T., Rogers, B. M., Xu, L., Wang, J. A., Magney, T., and Miller, C. E.: The Impacts of Climate and Wildfire on Ecosystem Gross Primary Productivity in Alaska, Journal of Geophysical Research: Biogeosciences, 126, 1–14, https://doi.org/10.1029/2020JG006078, 2021.

Magney, T. S., Bowling, D. R., Logan, B. A., Grossmann, K., Stutz, J., Blanken, P. D., Burns, S. P., Cheng, R., Garcia, M. A., Köhler, P., Lopez, S., Parazoo, N. C., Raczka, B., Schimel, D., and Frankenberg, C.: Mechanistic evidence for tracking the seasonality of photosynthesis with solar-induced fluorescence, Proceedings of the National Academy of Sciences of the United States of America, 116, 11 640–11 645, https://doi.org/10.1073/pnas.1900278116, 2019.

Magney, T. S., Barnes, M. L., and Yang, X.: On the Covariation of Chlorophyll Fluorescence and Photosynthesis Across Scales, Geophysical Research Letters, 47, 1–7, https://doi.org/10.1029/2020GL091098, 2020.

Moene, A. F. and Van Dam, J. C.: Transport in the atmosphere-vegetation-soil continuum, Cambridge University Press, 2014.

Monteith, J.: Solar Radiation And Productivity in Tropical Ecosystems, Society, 9, 747–766, 1972.

Muñoz Sabater, J.: ERA5-Land hourly data from 1981 to present, 10.24381/cds.e2161bac, 2019.

Porcar-Castell, A., Tyystjärvi, E., Atherton, J., Van Der Tol, C., Flexas, J., Pfündel, E. E., Moreno, J., Frankenberg, C., and Berry, J. A.: Linking chlorophyll a fluorescence to photosynthesis for remote sensing applications: Mechanisms and challenges, Journal of Experimental Botany, 65, 4065–4095, https://doi.org/10.1093/jxb/eru191, 2014.

Qu, S., Wang, L., Lin, A., Yu, D., Yuan, M., and Li, C.: Distinguishing the impacts of climate change and anthropogenic factors on vegetation dynamics in the Yangtze River Basin, China, Ecological Indicators, 108, 105 724, https://doi.org/10.1016/j.ecolind.2019.105724, 2020.

Rogelj, J., Shindell, D., Jiang, K., Fifita, S., Forster, P., Ginzburg, V., Handa, C., Kheshgi, H., Kobayashi, S., Kriegler, E., Mundaca, L., Séférian, R., and Vilariño, M.: Mitigation Pathways Compatible with 1.5°C in the Context of Sustainable Development. In: Global Warming of 1.5°C. An IPCC Special Report on the impacts of global warming of 1.5°C above pre-industrial levels and related global greenhouse gas emission pathw, IPCC special report Global Warming of 1.5 ºC, p. 82pp, https://www.ipcc.ch/site/assets/uploads/sites/2/2019/02/SR15{_}Chapter2{_}Low{_}Res.pdf, 2018.

Schimel, D., Stephens, B. B., and Fisher, J. B.: Effect of increasing CO2 on the terrestrial carbon cycle, Proceedings of the National Academy of Sciences of the United States of America, 112, 436–441, https://doi.org/10.1073/pnas.1407302112, 2015.

Schurgers, G., Ahlström, A., Arneth, A., Pugh, T. A., and Smith, B.: Climate Sensitivity Controls Uncertainty in Future Terrestrial Carbon Sink, Geophysical Research Letters, 45, 4329–4336, https://doi.org/10.1029/2018GL077528, 2018.

Smith, W. K., Fox, A. M., MacBean, N., Moore, D. J., and Parazoo, N. C.: Constraining estimates of terrestrial carbon uptake: new opportunities using long-term satellite observations and data assimilation, New Phytologist, 225, 105–112, https://doi.org/10.1111/nph.16055, 2020.

Song, L., Guanter, L., Guan, K., You, L., Huete, A., Ju, W., and Zhang, Y.: Satellite sun-induced chlorophyll fluorescence detects early response of winter wheat to heat stress in the Indian Indo-Gangetic Plains, Global Change Biology, 24, 4023–4037, https://doi.org/10.1111/gcb.14302, 2018.

Stol, J. and Kitchen, M.: Tumbarumba Flux Data Release 2022_v1 (Version 1.0) [Dataset], Terrestrial Ecosystem Research Network, https://doi.org/10.25901/esrb-5609, 2022.

Sun, H., Wang, J., Xiong, J., Bian, J., Jin, H., Cheng, W., and Li, A.: Vegetation Change and Its Response to Climate Change in Yunnan Province, China, Advances in Meteorology, 2021, https://doi.org/10.1155/2021/8857589, 2021.

Sun, W., Song, X., Mu, X., Gao, P., Wang, F., and Zhao, G.: Spatiotemporal vegetation cover variations associated with
585   climate change and ecological restoration in the Loess Plateau, Agricultural and Forest Meteorology, 209-210, 87–99,
https://doi.org/10.1016/j.agrformet.2015.05.002, 2015.

Sun, Y., Frankenberg, C., Jung, M., Joiner, J., Guanter, L., Köhler, P., and Magney, T.: Overview of Solar-Induced chlorophyll Fluorescence
(SIF) from the Orbiting Carbon Observatory-2: Retrieval, cross-mission comparison, and global monitoring for GPP, Remote Sensing of
Environment, 209, 808–823, https://doi.org/10.1016/j.rse.2018.02.016, 2018.

590   Turner, A., Köhler, P., Magney, T., Frankenberg, C., Fung, I., and Cohen, R.: Extreme events driving year-to-year differences in gross primary
productivity across the US, Biogeosciences Discussions, 1, 1–13, https://doi.org/10.5194/bg-2021-49, 2021.

Turner, A. J., Köhler, P., Magney, T. S., Frankenberg, C., Fung, I., and Cohen, R. C.: A double peak in the seasonality of California's
photosynthesis as observed from space, Biogeosciences, 17, 405–422, https://doi.org/10.5194/bg-17-405-2020, 2020.

United Nations: Conference of the Parties Twenty - second session Marrakech, 7 – 18 November 2016 Item X of the provisional agenda,
595   Aggregate effect of the intended nationally determined contributions: an update, 07126, 16–7126, http://unfccc.int/resource/docs/2016/
cop22/eng/02.pdf, 2016.

Van Schaik, E., Kooreman, M. L., Stammes, P., Gijsbert Tilstra, L., Tuinder, O. N., Sanders, A. F., Verstraeten, W. W., Lang, R., Cacciari, A.,
Joiner, J., Peters, W., and Folkert Boersma, K.: Improved SIFTER v2 algorithm for long-term GOME-2A satellite retrievals of fluorescence
with a correction for instrument degradation, Atmospheric Measurement Techniques, 13, 4295–4315, https://doi.org/10.5194/amt-13-
600   4295-2020, 2020.

Veefkind, J. P., Aben, I., McMullan, K., Förster, H., de Vries, J., Otter, G., Claas, J., Eskes, H. J., de Haan, J. F., Kleipool, Q., van Weele,
M., Hasekamp, O., Hoogeveen, R., Landgraf, J., Snel, R., Tol, P., Ingmann, P., Voors, R., Kruizinga, B., Vink, R., Visser, H., and Levelt,
P. F.: TROPOMI on the ESA Sentinel-5 Precursor: A GMES mission for global observations of the atmospheric composition for climate,
air quality and ozone layer applications, Remote Sensing of Environment, 120, 70–83, https://doi.org/10.1016/j.rse.2011.09.027, 2012.

605   Verma, M., Schimel, D., Evans, B., Frankenberg, C., Beringer, J., Drewry, D. T., Magney, T., Marang, I., Hutley, L., Moore, C., and Eldering,
A.: Effect of environmental conditions on the relationship between solar-induced fluorescence and gross primary productivity at an OzFlux
grassland site, Journal of Geophysical Research: Biogeosciences, 122, 716–733, https://doi.org/10.1002/2016JG003580, 2017.

Wang, S., Zhang, Y., Ju, W., Porcar-Castell, A., Ye, S., Zhang, Z., Brümmer, C., Urbaniak, M., Mammarella, I., Juszczak, R., and Folkert
Boersma, K.: Warmer spring alleviated the impacts of 2018 European summer heatwave and drought on vegetation photosynthesis,
610   Agricultural and Forest Meteorology, 295, 108 195, https://doi.org/10.1016/j.agrformet.2020.108195, 2020.

Wang, S., Li, R., Wu, Y., and Zhao, S.: Effects of multi-temporal scale drought on vegetation dynamics in Inner Mongolia from 1982 to 2015
, China, Ecological Indicators, 136, 108 666, https://doi.org/10.1016/j.ecolind.2022.108666, 2022.

Yang, J. and Huang, X.: The 30m annual land cover dataset and its dynamics in China from 1990 to 2019, Earth System Science Data, 13,
3907–3925, https://doi.org/10.5194/essd-13-3907-2021, 2021.

615   Zhang, L. and Schwärzel, K.: China's land resources dilemma: Problems, outcomes, and options for sustainable land restoration, Sustain-
ability (Switzerland), 9, https://doi.org/10.3390/su9122362, 2017.

Zhang, W., Wei, F., Horion, S., Fensholt, R., Forkel, M., and Brandt, M.: Global quantification of the bidirectional dependency between soil
moisture and vegetation productivity, Agricultural and Forest Meteorology, 313, https://doi.org/10.1016/j.agrformet.2021.108735, 2022.

Zhang, Y. and Ye, A.: Quantitatively distinguishing the impact of climate change and human activities on vegetation in mainland China with
620   the improved residual method, GIScience and Remote Sensing, 58, 235–260, https://doi.org/10.1080/15481603.2021.1872244, 2021.

Zhang, Y., Xiao, X., Zhang, Y., Wolf, S., Zhou, S., Joiner, J., Guanter, L., Verma, M., Sun, Y., Yang, X., Paul-limoges, E., Gough, C. M., Wohlfahrt, G., Gioli, B., and Tol, C. V. D.: On the relationship between sub-daily instantaneous and daily total gross primary production : Implications for interpreting satellite-based SIF retrievals, Remote Sensing of Environment, 205, 276–289, https://doi.org/10.1016/j.rse.2017.12.009, 2018.